Rowan University
Rowan Digital Works

Theses and Dissertations

9-27-2022

Low Temperature Dielectric Strength of Polyimide-Silica Nanocomposites for Applications in High-Temperature Superconducting Cables

Michael John McCaffrey
Rowan University

Follow this and additional works at: https://rdw.rowan.edu/etd

Part of the Electrical and Computer Engineering Commons

Recommended Citation
McCaffrey, Michael John, "Low Temperature Dielectric Strength of Polyimide-Silica Nanocomposites for Applications in High-Temperature Superconducting Cables" (2022). *Theses and Dissertations*. 3059.
https://rdw.rowan.edu/etd/3059

This Thesis is brought to you for free and open access by Rowan Digital Works. It has been accepted for inclusion in Theses and Dissertations by an authorized administrator of Rowan Digital Works. For more information, please contact graduateresearch@rowan.edu.

LOW TEMPERATURE DIELECTRIC STRENGTH OF POLYIMIDE-SILICA NANOCOMPOSITES FOR APPLICATIONS IN HIGH-TEMPERATURE SUPERCONDUCTING CABLES

by

Michael John McCaffrey

A Thesis

Submitted to the
Department of Electrical & Computer Engineering
College of Engineering
In partial fulfillment of the requirement
For the degree of
Master of Science in Electrical and Computer Engineering
at
Rowan University
April 28, 2022

Thesis Chair: Robert Krchnavek, Ph.D., P.E., Professor, Department of Electrical and Computer Engineering

Committee Members:
Wei Xue, Ph.D., Associate Professor, Department of Mechanical Engineering
John Schmalzel, Ph.D., P.E., Professor, Department of Electrical and Computer Engineering
Jie Li, Ph.D., Associate Professor, Department of Electrical and Computer Engineering

© 2022   Michael John McCaffrey

Dedications

This work is dedicated to my wife, Jenna, for her unwavering encouragement throughout this journey; my parents, Larry and Ilona, for believing in me; and my children, June and Michael, for motivating me to be my best, always.

Acknowledgments

I must first thank my advisor, Dr. Robert Krchnavek for providing me with the chance to conduct this research, and for his wisdom and patience throughout. I am very fortunate to have had the opportunity to perform this work under his guidance and will continue to learn and draw from this experience for many years.

Thanks to Dr. Wei Xue, for sharing his experience, his attentiveness. and his support in the research laboratory; and to Dr. Jacob Kephart and the Applied Superconductivity team at the Naval Surface Warfare Center in Philadelphia for their advice and resources. Thanks to my fellow graduate students working on this project, Joseph Nalbach, Harrison Hones, and Jordan Cook, for their great work and companionship.

Abstract

Michael John McCaffrey
LOW TEMPERATURE DIELECTRIC STRENGTH OF POLYIMIDE-SILICA NANOCOMPOSITES FOR APPLICATIONS IN HIGH-TEMPERATURE SUPERCONDUCTING CABLES
2021-2022
Robert Krchnavek, Ph.D.
Master of Science in Electrical and Computer Engineering

Gaseous helium is often considered as an alternative to liquid nitrogen to cool modern high-temperature superconducting cables in support of increased power capacity and/or reduction of required cable size. However, the small size of helium molecules and relatively poor dielectric strength of helium gas create challenges which limit the usefulness of modern cable dielectrics. Continuous dielectric coatings have been considered as an alternative to traditional lapped tape dielectrics to support gaseous helium refrigerants, but unmatched thermal contraction between the coating and cable components would induce failures due to mechanical stress. Composite materials have been considered as a means of matching rates of thermal expansion to that of superconducting cables while retaining excellent withstanding against strong electric fields. Polyimide/silicon dioxide nanocomposites are a promising candidate for this application and are examined as such in this work. Nanocomposite films of various filler concentrations up to 7% were produced and tested for their dielectric strength at both room temperature and approximately 90 K. Despite a slight reduction in dielectric strength with increased nanoparticle concentrations at room temperature, the results suggest that polyimide provides ample dielectric strength as a composite matrix in superconducting cable dielectrics.

Table of Contents

Abstract v

List of Figures x

List of Tables xiii

Chapter 1: Introduction 1

Chapter 2: Background 6

2.1 High Temperature Superconductivity 6

2.1.1 History 6

2.1.2 The Critical Surface 7

2.1.3 HTS Cable Systems 9

2.2 Refrigerants in HTS Systems 12

2.2.1 Conventional Refrigerants 12

2.2.2 Gaseous Helium 12

2.3 HTS Dielectrics 15

2.3.1 Dielectric Application Methods 16

2.4 Dielectric Breakdown 19

2.4.1 Overview 19

2.4.2 Mechanisms 20

2.4.3 Breakdown, Sparkover, and Flashover 24

2.4.4 Paschen's Law 25

Table of Contents (Continued)

2.4.5 The Weibull Distribution ... 31

2.5 Nanocomposites ... 33

2.5.1 Overview ... 33

2.5.2 Tuning the Coefficient of Thermal Expansion with Nanoparticles ... 34

2.6 Polyimide/Silica Nanocomposites ... 35

2.6.1 Polyimide ... 36

2.6.2 Silica ... 37

2.7 Relevant Previous Works ... 38

2.7.1 Electric Field Enhancement with Composite Filler Addition ... 39

2.7.2 Dielectric Strength of Epoxy/TiO_2 Nanocomposites at LN Temperatures ... 42

2.7.3 Effects of Particle Dispersion on Dielectric Withstand Capability ... 43

2.7.4 Room Temperature Dielectric Strength vs. Filler Concentration in PI/SiO_2 Nanocomposites ... 44

2.7.5 Cryogenic Dielectric Strength of Polyimide ... 46

2.7.6 Cryogenic CTE vs. Filler Concentration in PI/SiO_2 Nanocomposites at Low Temperatures ... 49

Chapter 3: Experimental Methods ... 51

3.1 Sample Preparation and Verification ... 51

3.1.1 Film Preparation ... 51

3.1.2 Scanning Electron Microscopy and Particle Analysis ... 54

Table of Contents (Continued)

3.2 Room Temperature Dielectric Strength Testing 54

3.2.1 System Overview 54

3.2.2 Test Procedure 57

3.2.3 Puncture Verification and Hole Geometry Analysis 61

3.3 LN-Cooled Testing 61

3.3.1 Environment 62

3.3.2 LN Test Fixture 63

Chapter 4: Results and Discussion 66

4.1 Sample Preparation 66

4.1.1 Particle Dispersion 67

4.2 Room Temperature Dielectric Strength 71

4.2.1 Electrode Simulation 71

4.2.2 Control Measurements 74

4.2.3 Kapton PI vs. Lab-Made PI 74

4.2.4 Dielectric Strength vs. Silica Concentration 75

4.2.5 Breakdown Microscopy 78

4.2.6 Geometric Analysis of Perforation Regions 79

4.3 Low Temperature Dielectric Strength 82

4.3.1 Low Temperature Control Measurements 82

Table of Contents (Continued)

4.3.2 Low Temperature Nanocomposite Dielectric Strength 82

4.3.3 Dielectric Strength vs. Silica Concentration vs. Temperature 83

4.3.4 SEM Imaging of Low Temperature Dielectric Failures 86

4.4 Recommendations for Future Work 88

4.4.1 Nanocomposite Generation 88

4.4.2 Spin Coating 89

4.4.3 Dielectric Strength Testing 90

4.4.4 Helium-Cooled Dielectric Strength Tests 92

Chapter 5: Conclusion 93

References 95

List of Figures

Figure Page

Figure 2.1. Generic Resistivity against Temperature in Normal Conductor and Superconductor 6

Figure 2.2. Discovery Timeline of Record-breaking High Temperature Superconductors............ 7

Figure 2.3. Critical Surface of Superconductivity 9

Figure 2.4. HTS Cable Configurations 10

Figure 2.5. Exposed Three-Phase HTS Cable Layers............ 11

Figure 2.6. Helium and Nitrogen Phase States Against Temperature 13

Figure 2.7. 15 Years of Crude Helium Prices in 1998 Dollars............ 14

Figure 2.8. 15 Years of U.S. Helium Stocks............ 14

Figure 2.9. Lapped-Tape Dielectric Application for HTS Cables............ 16

Figure 2.10. Butt Gaps Between Lapped-Tape Dielectric Layers............ 17

Figure 2.11. Breakdown Path Through Helium-Spanned Dielectric Gaps............ 17

Figure 2.12. Unequal Thermal Contraction Between Cable Core and Dielectric 19

Figure 2.13. Breakdown Field Strength vs. Inception Time with Likely Associated Mechanisms 21

Figure 2.14. Breakdown Due to Electrocompressive Forces............ 22

Figure 2.15. Capacitor Model of Dielectric Material Defects 23

Figure 2.16. Comparison of Breakdown, Flashover, and Sparkover............ 25

Figure 2.17. Paschen's Curve for Various Gases 26

Figure 2.18. Generic Relationship Between Incident Particle Energy and SEEC............ 28

Figure 2.19. Effects of Pressure and Gap Distance on Free Electron Collisions............ 30

Figure 2.20. Cumulative Density Function for Nonspecific Weibull Distribution 32

Figure 2.21. Thermal Contraction in Polyimide, Silica Glass, and Copper at Low Temperatures............ 35

List of Figures (Continued)

Figure Page

Figure 2.22. Imidization with Atoms Removed During Reaction Highlighted 37

Figure 2.23. Model of a PEA System for Measuring Dielectric Space Charge Distribution 40

Figure 2.24. Electric Field Strength in Epoxy/TiO2 Composite Samples 41

Figure 2.25. Dielectric Strength of Epoxy/TiO2 Nano/Micro (a/b) Composites 42

Figure 2.26. Dielectric Strength of Epoxy/TiO2 Composites and Pure Epoxy at 77 K ... 43

Figure 2.27. Dielectric Strength vs. Dispersion Quality in PE/MMT Nanocomposites ... 44

Figure 2.28. Dielectric Strength vs. Filler Concentration in PI/SiO2 Nanocomposites ... 45

Figure 2.29. PI Dielectric Strength at Temperatures Between 5 K and Room Temperature 48

Figure 2.30. CTE vs. Temperature and Filler Concentration for PI/SiO2 Nanocomposites 50

Figure 3.1. Spin Coating Speed Profile 53

Figure 3.2. Temperature Profiles for Curing Polyamide and PI Films 53

Figure 3.3. Room Temperature Dielectric Strength Testing Fixture 55

Figure 3.4. Vitrek 955i Hipot Tester 56

Figure 3.5. Room Temperature Dielectric Strength Testing System Diagram 57

Figure 3.6. Test Procedure Flow Chart 60

Figure 3.7. LN Testing Chamber Designed for Low-Temperature Measurements 62

Figure 3.8. LN-Cooled Testing Fixture for Testing Four Samples at Once 64

Figure 4.1. Photo of a PI/Silica Nanocomposite Film on a Lab Slide 66

Figure 4.2. Thickness Distribution for Room Temperature Test Samples 67

Figure 4.3. SEM Image of Composite Film with 7% SiO2 by Weight 68

Figure 4.4. Particles Identified with MATLAB's Image Processing Toolbox 68

List of Figures (Continued)

Figure Page

Figure 4.5. Particle Count in Each Size Regime Among Particles Circled in Figure 4.4 69

Figure 4.6. Distribution of Silica Pixels in Figure 4.3 Among Particle Size Regimes 70

Figure 4.7. Simulated Electric Field Strength Across the Electrode Contact Area 73

Figure 4.8. Simulated Electric Field for Electrodes Loaded with Polyimide Film........... 73

Figure 4.9. Dielectric Strength for Kapton Film at Room Temperature........... 74

Figure 4.10. Lab-Made Polyimide Dielectric Strength Compared to Kapton 75

Figure 4.11. Dielectric Strength vs. Silica Concentration for PI/SiO2 Films........ 76

Figure 4.12. Dielectric Strength vs. Silica Concentration for PI/SiO2 Films........ 77

Figure 4.13. Inner (left) and Outer (right) Regions of a Dielectric Breakdown Puncture 78

Figure 4.14. SEM (left) and Optical (right) Captures of a Dielectric Breakdown Puncture 79

Figure 4.15. *Dielectric Breakdown Hole Size Against SiO_2 Concentration* 80

Figure 4.16. Hole Size vs. Dielectric Strength, Breakdown Voltage, and Sample Thickness 81

Figure 4.17. Dielectric Strength for Kapton Film at Low Temperatures........ 82

Figure 4.18. Results of Low Temperature Dielectric Strength Testing 83

Figure 4.19. Comparison Between Low-Temperature and Room-Temperature Results........ 84

Figure 4.20. Standard Deviation for Dielectric Strength Measurements........ 85

Figure 4.21. Breakdown Holes Formed at Room (top) and Low Temperatures (middle, bottom)........ 87

List of Tables

Table Page

Table 2.1. Properties from Kapton HN Datasheet 36

Table 2.2. Select Properties of Silicon Dioxide 38

Table 2.3. Dielectric Strength of PI/SiO2 Nanocomposites vs. Silica Concentration 46

Table 3.1. Materials Required for Silica Sol-Gel 51

Table 4.1. Dielectric Strength at Room and Low Temperature 84

Chapter 1

Introduction

Since its discovery in the early 20th century, superconductors—materials which at low temperatures can carry electrical currents free from resistance—have had major impacts on several industries and technologies [1, 2] The lossless power transmission and magnetic fields achievable through superconductivity have enabled a number of innovations leading to vital instruments, tools, and mechanisms [3]. Today, for example, superconductors are essential components of MRI machines, electromagnetic railguns, and particle accelerators [4, 5]. More recently emerging applications of superconductivity span a large number of fields such as digital electronics, microwave filters and antennas, and aircraft propulsion [6, 7, 8, 9].

Along with ongoing efforts to improve existing applications of superconductivity, the trend of its adoption into new domains sustains an upward pressure on the limits of superconductor technology [10]. Much of this pressure is relieved in the exploration of a fundamental attribute of superconductive materials: a multi-dimensional relationship between superconductivity, temperature, electrical current density, and magnetic fields known as the *critical surface* [11]. This critical surface defines essential trade-offs, where for example a lower temperature allows for greater current densities or for the presence of stronger magnetic fields. Similarly, a material can remain superconductive at higher temperatures if it is carrying lower current densities.

Some materials, known as *high-temperature superconductors*, exhibit a critical temperature significantly higher than that of the earliest superconductive materials discovered. Though there is no clearly defined temperature threshold for "high

temperature" in superconductivity, the term can be traced at least as far back as the 1986 discovery of a material exhibiting superconductivity at 35 K [12]. Today, common HTS materials can reach superconductivity when cooled by liquid nitrogen (LN), which boils at atmospheric pressure near 77 K [13]. The low cost of LN as a refrigerant in HTS systems allows for its aforementioned adoption into a breadth of industries including healthcare, defense, and transportation.

An HTS cable transmits power without resistive losses in DC, AC, and three-phase configurations [1, 2, 4]. With superconductive cables, power can be passed over long distances in high capacity without the dissipation of energy that occurs in conventional conductors [5]. For applications which justify the use of HTS cables, the costs of installation and cooling are outweighed by savings due to the increased power transmission efficiency, or through enabling previously unreachable mechanisms. As one instance, some applications call for the use of HTS cables due to their requirements for instant extreme power delivery between subsystems which can be separated by considerable distances [5, 14].

Of course, implementations of HTS cable systems in practice are not only subject to limitations inherent to the superconductor material, but also to those defined by their application. A clear example is the constraint that an installation environment can impose on the maximum diameter and weight of the cable. Along with the space and support requirements for a long, thick, and heavy cable, the cost of installation for such an unwieldy cable can be prohibitive. This fact provides an incentive to improve the technology such that HTS cables can be made smaller and thus more easily drawn through tight and labyrinthine systems.

One clear path to decreasing an HTS cable's diameter is through increasing its current carrying capacity [15]. This can be achieved by decreasing the operating temperature, and thus moving deeper into the material's critical surface [2, 11]. The adoption of gaseous helium (GHe) as an HTS cryogen in the place of now ubiquitous LN cooling can bring within reach lower temperatures and increase the critical current density of the HTS material [16]. The expanded capacity for carrying electrical current per unit cross-sectional area allows for a smaller cable and therefore a less expensive cable installation.

Currently, the potential adoption of GHe as a coolant in HTS systems is impeded by a lack of suitable dielectrics. The typical HTS cable dielectric which isolates the superconductive wire from other cable components is applied in the form of a tape that is wrapped around the wire along its length in an overlapping fashion [17, 18]. This is an adequate strategy in LN-cooled systems and is reinforced by the electric field withstanding capability of nitrogen [19]. However, in the context of a GHe-cooled HTS cable, the overlapping layers of tape are a debilitating weakness. From the perspective of helium—the smallest molecule on Earth in terms of atomic radius—the gaps that form between these overlapping layers are gigantic and can be passed through freely [20]. This effectively allows the GHe to act as a weakness in the dielectric through the entire cable length. As a result, the dielectric's ability to isolate unlike charges is reduced to that of helium, which is less than one twentieth that of air [19]. Consequently, this negates the dielectric's utility almost entirely.

This problem could be solved through the extrusion of a continuous dielectric coating onto the superconductor wire. Without the gaps that are produced in the lapped

tape scheme, helium would have no opportunity to bridge between conductors and create weak points in the dielectric. Still, this strategy is not without drawbacks of its own. All materials have some degree to which they change size with temperature, a feature which would be expressed by the low temperatures required for an HTS cable's operation [21]. This property varies broadly from material to material, and physically coupled materials which change size at different rates can incur stresses that lead to mechanical failures [22]. For such a failure in the dielectric coating of an HTS cable, helium will rush to fill any newly created opening, and again the dielectric's effectiveness is compromised.

Although an uneven change in size between cable components could be catastrophic to an HTS cable, this would not be the case when the system grows and shrinks at one unified rate. If a dielectric material could be created to mimic the thermal expansion and contraction of the rest of the cable assembly, it could be coated onto the conductor as an insulator for smaller, more easily installed GHe-cooled HTS cables.

Composite materials provide avenues for engineers which can coarsely combine desirable attributes or mitigate drawbacks of homogeneous materials [23]. Moreover, nanocomposites enable more careful adoption of filler material properties while largely preserving behaviors of the host material [24, 25]. Since their relatively recent emergence, nanocomposites are being employed in a growing number of novel applications, and are creating new inroads to many longstanding and modern challenges [26].

This work describes the development and testing of a novel polyimide (PI) / silica (SiO_2) nanocomposite material being engineered to match the coefficient of thermal

expansion of a copper HTS cable core for application as a dielectric coating. PI/SiO_2 nanocomposites with filler concentrations ranging from 1 to 7% were produced through an in situ process. The materials were spin-coated into film specimens of approximately 15 μm in thickness and then cured. Using computer vision techniques applied to scanning electron microscope images, silica particle sizes were estimated and then statistically analyzed. Under the guidance of ASTM standard D3755 for acquiring DC dielectric strength of materials, DC electrical stresses were applied across the film samples to the point of dielectric breakdown both at room temperature and at 90 kelvin. After dielectric failure, perforations produced by breakdown were analyzed geometrically under an optical microscope. The data recorded in this work were analyzed and the materials assessed for their suitability as candidates for additional testing down to 40 kelvin, and for their practicality as dielectric coatings in HTS cables.

Chapter 2

Background

2.1 High Temperature Superconductivity

The term superconductivity refers to the state of a material in which its resistivity is zero. That is, electrons can flow through the material without resistance, and thus without dissipating any energy. An example of the transition to superconductivity is illustrated in Figure 2.1. In the figure, the immediate shift to zero resistance is contrasted with the continuous approach toward some minimum non-zero resistance value with decreasing temperature. These two curves represent examples of materials with and without, respectively, the ability to exhibit superconductivity.

Figure 2.1

Generic Resistivity against Temperature in Normal Conductor and Superconductor

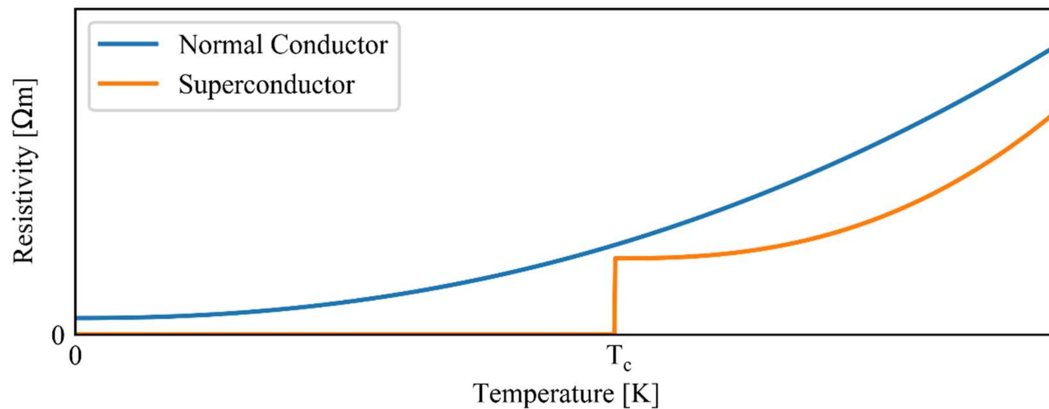

2.1.1 History

The first documented manifestation of superconductivity came through the low temperature characterization of mercury in 1911 by Heike Kamerleigh Onnes [1]. During

his research with liquid helium, the physicist found that the metal's electrical resistance fell to zero at the temperature of 4.2 K. Soon after, metals were discovered to exhibit superconductivity at warmer temperatures, and they have since become predecessors to today's multitude of high-temperature superconductors.

The discovery of yttrium barium copper oxide's (YBCO) superconductive state in 1987 was the first above the boiling temperature of LN at 92 K [27]. It, along with bismuth strontium calcium copper oxide (BSCCO) and a number of other copper oxide materials (see Figure 2.2), ushered in the modern presence of HTS in society. Very recently, researchers claim to have observed superconductivity at temperatures as high as 250 K, only 50 K below room temperature [28].

Figure 2.2

Discovery Timeline of Record-breaking High Temperature Superconductors

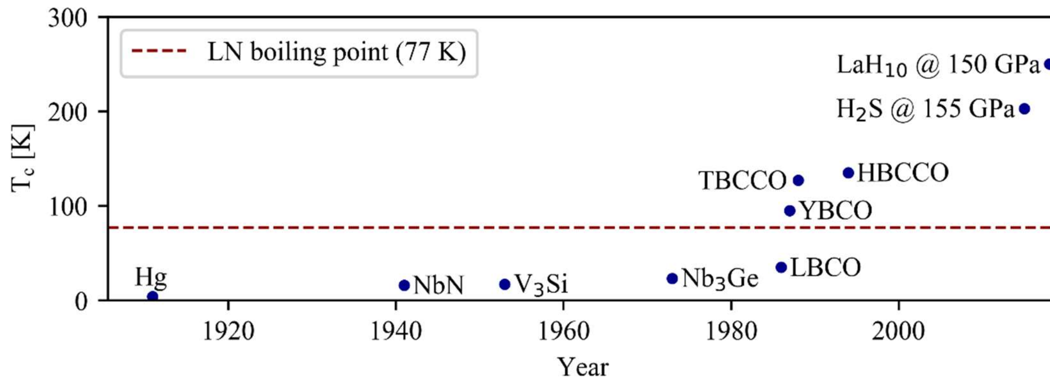

2.1.2 The Critical Surface

The underlying mechanisms of superconductivity are a complex topic that requires an understanding of various topics in quantum physics. It is beyond the scope of this work and will not be discussed in detail. However, there are some consequences of

these mechanisms that are critical to understand when considering the applications of HTS materials. Predominant among these consequences is the critical surface.

Superconductivity exists as a binary state of materials which can exhibit it. A superconductor will enter and exit this state depending primarily on three conditions: the temperature of the material (T), the presence of magnetic fields (H), and the density of electrical current passing through the materials (J). For each of these conditions exists a critical value above which the material is broken out of the superconductive state. These values and their distributed relationships form a three-dimensional threshold which defines the bounds of the material's zero-resistance capabilities [14, 29].

This critical surface, of which a nonspecific example is shown in Figure 2.3, is both a fundamental constraint on HTS applications as well as a guide for their optimization. Since the emergence of superconductor technology, the critical surfaces of common superconductor materials have been revealed through empirical methods. This data and the limits it prescribes can be leveraged for optimization as necessitated by the target application.

Figure 2.3

Critical Surface of Superconductivity

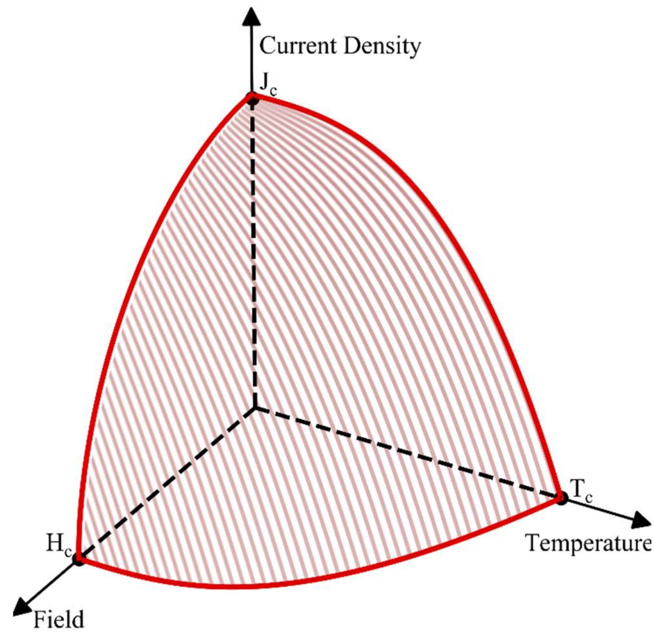

The critical values of T_c, H_c, and J_c are absolute maximum conditions for the quantities that they represent that will allow for superconductivity. If one of these values is reached or exceeded due to the surrounding environment or through consequences of operation, there is no tolerance for any nonzero conditions for either of the other two factors, and thus superconductivity cannot be achieved. However, when operating below all three critical values, there is room to manipulate trade-offs between them and further improve the utility of the material.

2.1.3 HTS Cable Systems

The exact architecture of HTS cables can vary widely according to the requirements of an application. Typically, as shown in Figure 2.4, these cables house between one and three conductors, and multi-conductor cables can exist in either

concentric or multi-core configurations [30, 31]. Here, a generic three-phase concentric cable and its components will be examined.

Figure 2.4

HTS Cable Configurations

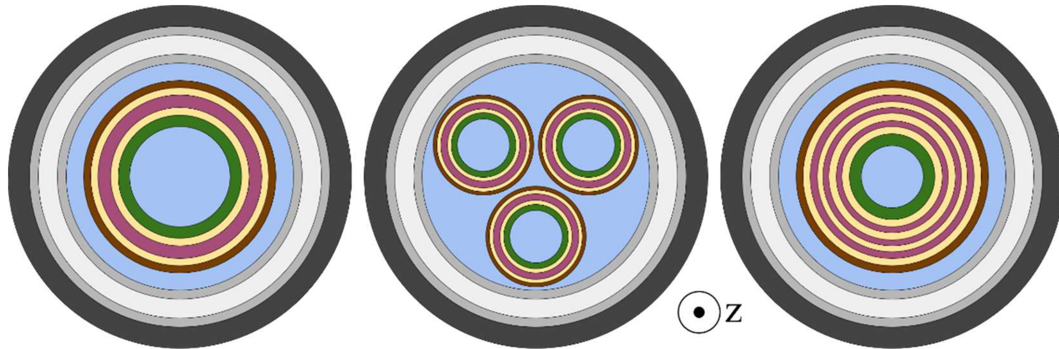

The outermost layer of the cable is simply a mechanically protective coating typically made of PVC or similar material. Inside of that exists a cryostat comprised of metal (typically steel) tubes which surround a thermally insulating vacuum. This stack serves to prevent heat from being pulled into the chilled inner layers. Just within the cryostat runs the returning refrigerant. Within that often lies a neutral copper screening layer that provides protection from external fields. Then, depending on the cable configuration, a series of insulating dielectric and HTS tape layers comprise the superconductive functionality. Finally, a section of copper tubing acts as the supportive cable former or core, and within that lies the refrigerant inlet. While this example outlines many common components of an HTS cable, many configurations exist with each their own distinctive features. An example of an HTS cable with three concentric conductors can be found in Figure 2.5.

Figure 2.5

Exposed Three-Phase HTS Cable Layers

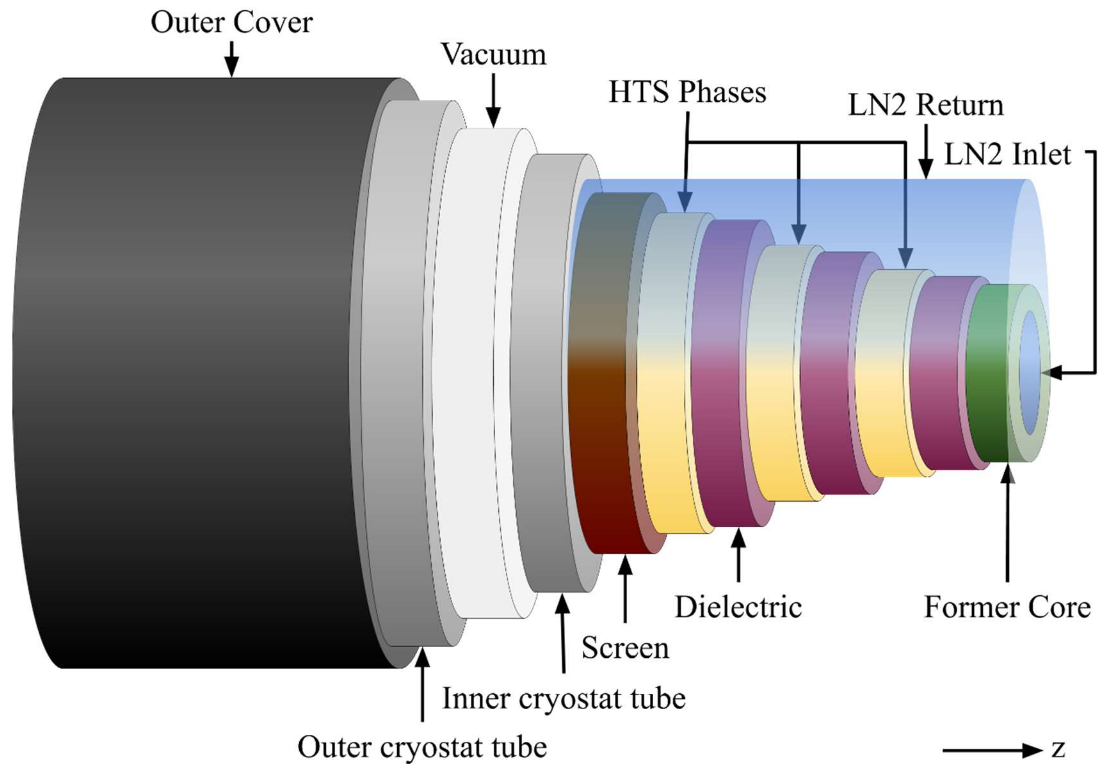

The superconductive layers of these cable systems are comprised of many HTS tapes or wires which are wound along the length of the cable. The coiled geometry of the conductors provides a benefit to the cable design in that adjacent HTS phases can be wound in opposite directions, and the mutual effects between them can improve performance. Another benefit of this configuration is relief from stresses due to the change in size and shape from handling, cooling, and heating the cable.

2.2 Refrigerants in HTS Systems

2.2.1 Conventional Refrigerants

Many HTS systems are cooled with LN. Its boiling point of 77 K is high enough to adequately cool many HTS materials in common applications, and it is relatively inexpensive to obtain. However, LN comes with considerable drawbacks which limit its practicality. First, its range of operating temperatures is fairly small; LN at atmospheric pressure will boil at 77 K and freeze at 63 K. Second, nitrogen expands at 700 to 1 when transitioning from liquid to gas. The implications of these two properties are significant regarding the convenience, cost, and safety of LN storage.

Liquid helium (LHe) is also a common coolant in cryogenic systems for superconductor applications. However, it requires very low temperatures with a boiling point of 4.1 K at 1 atm. Usually only for applications which call for very strong magnetic fields can the costs of implementing a LHe-cooled system be justified.

2.2.2 Gaseous Helium

A third alternative is gaseous helium (GHe), which as an HTS coolant has the potential to fill many of the gaps left by traditional ones. As shown in Figure 2.6, the range of temperatures in which gaseous helium maintains its gaseous state is far wider than that of LN or LHe in their liquid states. At atmospheric pressures, GHe can be cooled down near its boiling point of 4.1 K or stored at room temperature, and between the two will undergo no phase change. GHe offers clear benefits due to its wide range of operating temperatures.

Figure 2.6

Helium and Nitrogen Phase States Against Temperature

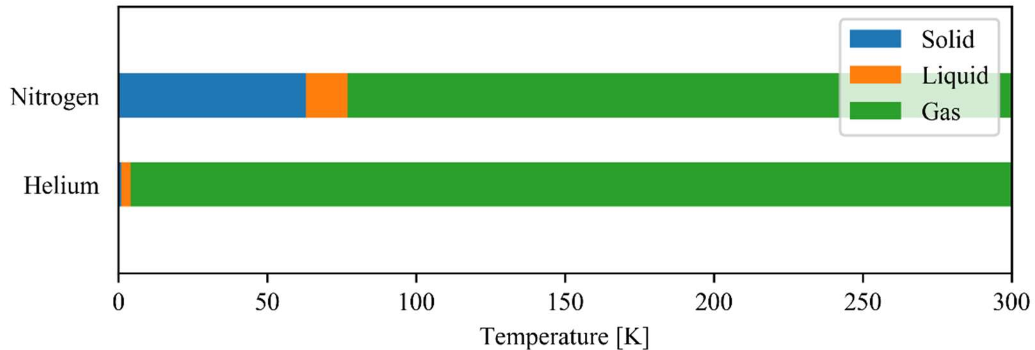

GHe can reach much lower temperatures than the freezing point of LN. As a consequence, cooling an HTS material with GHe instead of LN enables the operating temperature of the cable to extend deeper under its critical surface along the temperature axis. Referring to Figure 2.3, it is clear that this would create additional headroom for stronger magnetic fields or increased current density.

Second, helium is stable in its gaseous phase for temperatures above room temperature, meaning that it can be cooled for use as a refrigerant in an HTS system and stored at room temperature when not in use. Unlike LN, there is no phase change or significant change in volume to be encountered when going between room and cryogenic temperatures. Another consequence of this is that LN will boil off in storage over time, which leads to inevitable financial losses ideally not present in GHe systems. These properties make storage and transportation of GHe somewhat easier than that of LN.

The benefits of GHe as a refrigerant in HTS systems come with some notable drawbacks. For example, LN is inexpensive to acquire and can be conveniently generated

on-site with commercially available machines. On the other hand, helium is significantly more expensive, and as shown in Figure 2.7, its price is on the rise. This increase in price is tied to another issue with helium: it is in short supply. Data from the U.S. Bureau of Land Management, shown in Figure 2.8, highlight decreasing helium reserves for the past 15 years [32].

Figure 2.7

15 Years of Crude Helium Prices in 1998 Dollars

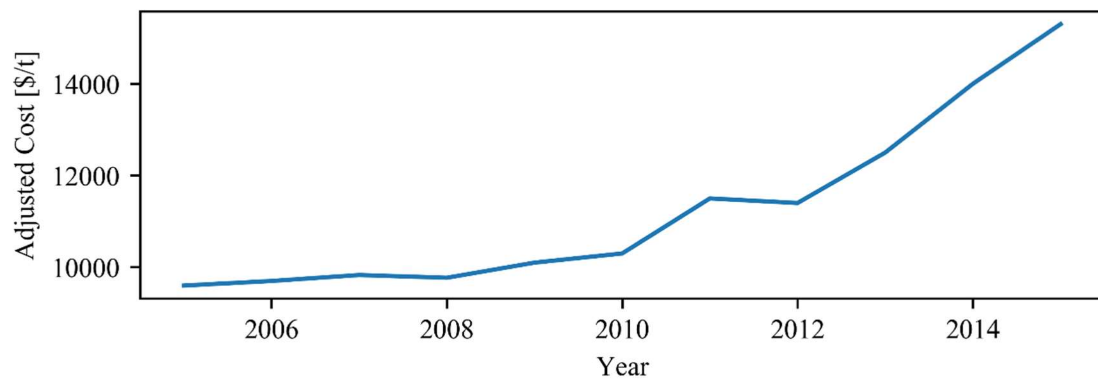

Figure 2.8

15 Years of U.S. Helium Stocks

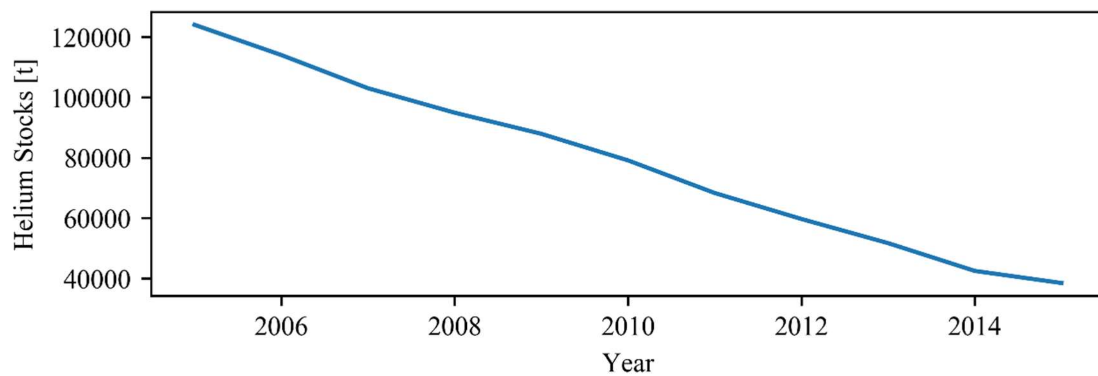

Another consideration that must be made in the context of HTS cables is the ability for the coolant to pass through small openings. This property is tied closely to the Van der Waals radius, which approximates the radius of a hard shell representative of the nearest point that another atom may approach. For nitrogen, the Van der Waals radius r_w is 155 pm [20]. It is also diatomic, which nearly doubles its r_w. Further, in its liquid state, nitrogen is subject to surface tension which would increase the minimum size of an opening through which it could pass. Ultimately, the ability to pass through small gaps is less of an issue in LN anyway, because of its superior dielectric withstand capability. As will be elucidated in the next sections, the dielectric strength of a coolant is a notable feature in the context of HTS cables. LN is superior in this respect, having the ability to withstand electric fields of 160 kV/mm [33].

Helium, on the other hand, is not a diatomic element, and its value for r_w is 140 pm. In its gaseous form, it is not subject to surface tension. The combination of these properties makes helium the most elusive of all gases, with the ability to diffuse, effuse, and adsorb through and into smaller gaps and denser materials than that of any other. Helium is also much weaker against electric fields; its dielectric strength is merely 15% that of nitrogen [19]. This is a critical consequence when considering the trade-offs between helium and nitrogen as coolants in an HTS cable.

2.3 HTS Dielectrics

Dielectrics in HTS cables are necessary to isolate the superconductor layers from each other as well as from cryostat tubes, copper cores, and screening conductors. They can be made of reinforced plastics, epoxies, LN-impregnated papers, or other polymer materials, and are desired to have a high dielectric strength and good flexibility [30].

2.3.1 Dielectric Application Methods

2.3.1.1 Lapped Tape. Dielectric layers are traditionally applied to HTS cables in a lapped-tape configuration. A tape of the dielectric material is wrapped around the cable such that it is overlapping on itself, as illustrated in Figure 2.9. The tape winds around the cable along the entire length, creating a barrier between the two adjacent layers. This strategy works well for LN-cooled systems. For one reason, the overlaps between the layers of dielectric tape allow it to contract without exposing the surrounding layers to one another. Second, it is relatively easy to apply.

Figure 2.9

Lapped-Tape Dielectric Application for HTS Cables

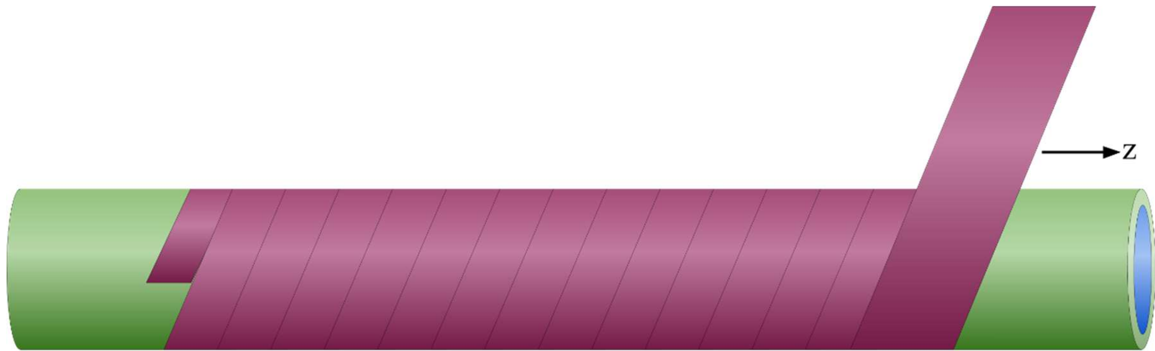

However, lapped-tape dielectrics would be rendered useless if they were used in GHe-cooled cables. This is due to the fact that the surfaces of the overlapping layers are not perfectly adjacent. In between the layers exist butt gaps which are on the order of 100 μm wide. A simplified illustration of butt gaps in between overlapping dielectric layers can be seen in Figure 2.10. For a helium atom, the size of the gap is vast, and can be passed through easily. When this is coupled with the relatively low dielectric strength

of helium, the dielectric layer is laced with dielectrically weak links throughout the entire cable length, creating many potential paths for dielectric breakdown (See Figure 2.11).

Figure 2.10

Butt Gaps Between Lapped-Tape Dielectric Layers

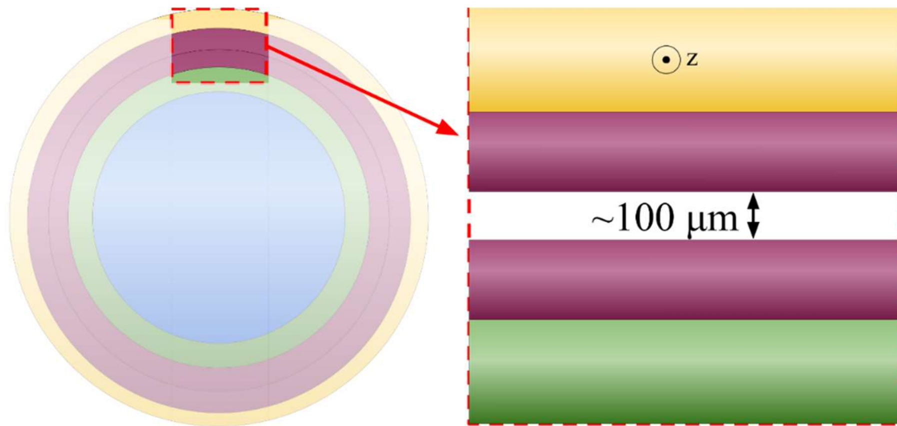

Figure 2.11

Breakdown Path Through Helium-Spanned Dielectric Gaps

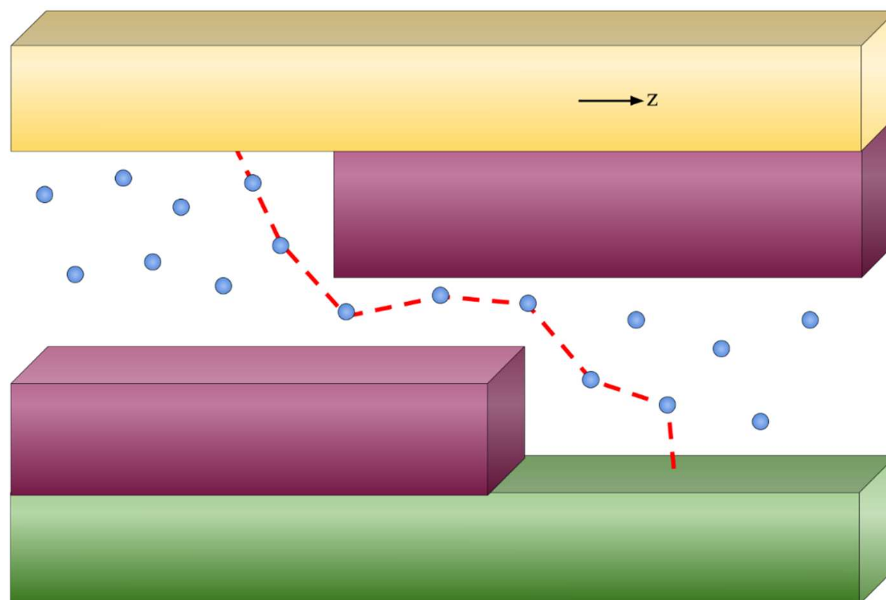

2.3.1.2 Extruded Polymers. As an alternative to lapped-tape application, a dielectric material can be applied as a continuous extruded polymer. With this method, the dielectric has no gaps through which helium can escape. Although the application process can be relatively more complicated than in lapped tapes, it is a potential path forward for dielectric layers in GHe-cooled HTS cables.

However, when cooled to low temperatures, the dielectric layer and the rest of the cable assembly will shrink. The rates of contraction for each material—governed by their coefficients of thermal expansion (CTE)—vary significantly [21]. While most of the HTS cable layers have shapes with some built-in strain relief in response to changes in size, the copper cable former and the extruded dielectric have no such virtue. Instead, the CTE mismatch would produce different rates of contraction between those two components (See Figure 2.12), and lead to stresses which could in turn cause mechanical failures in the dielectric [22]. Cracks produced by these failures would be filled with the dielectrically weak gaseous helium, again resulting in weaknesses prone to dielectric breakdown throughout the cable.

Figure 2.12

Unequal Thermal Contraction Between Cable Core and Dielectric

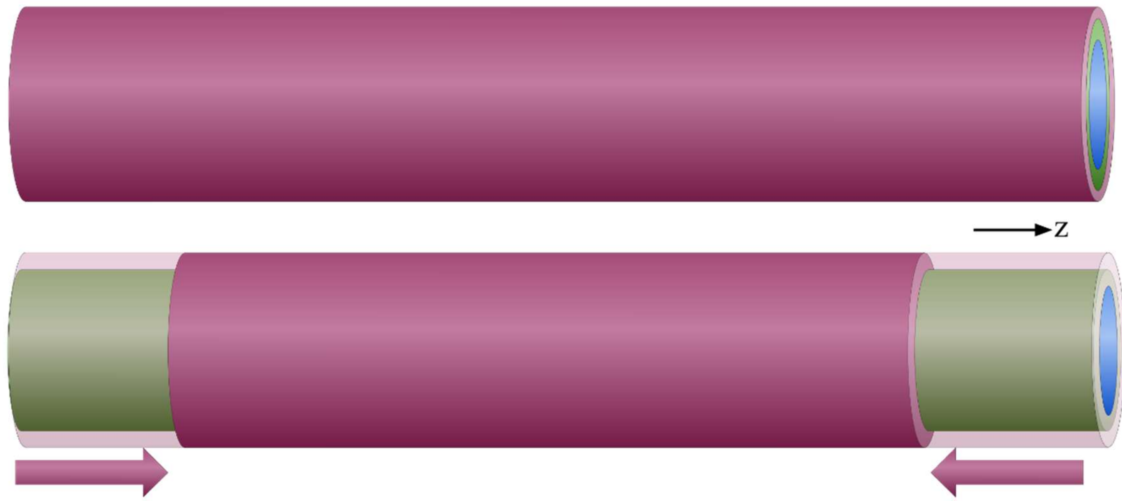

2.4 Dielectric Breakdown

2.4.1 Overview

In electrical conductors, electrons in nonuniform charge distributions can move freely toward equilibrium with little loss of energy. For superconductors, these losses are zero. On the other hand, resistive materials transfer electrons less readily, and insulators have virtually no charge carrying ability. For objects made of electrically insulating materials, differing charges on opposing sides cannot move to reach equilibrium. Instead, the electric fields which motivate the charges to move are sustained across the object. This electric field can cause a number of stresses, damages, and other degradation which can ultimately cause the object to fail in maintaining the separation of charges. This failure, known as dielectric breakdown, is a central concern of those who design cables, transformers, and other medium to high voltage components and systems.

Materials are characterized for their resistance to dielectric breakdown in the form of a quantity known as *dielectric strength*. This quantity is expressed with units of electric field strength: volts per meter, or more popularly as kilovolts per millimeter or volts per mil. Dielectric strength is determined through the application of a voltage across a material. A high enough voltage will discharge through the material in a breakdown event. This *dielectric withstand voltage* (DWV) can be combined with the measured thickness of the material to obtain the dielectric strength of the material. Typically, one test is not sufficient for generalization of a material; an average of five tests is prescribed by ASTM D3755 [34].

2.4.2 Mechanisms

For this work, it is vital to understand the different mechanisms which can lead to a dielectric breakdown, and to then establish confidence that the mechanism that can be attributed to causing a breakdown event is known. To maintain comparable results, it is desirable to control as many variables as possible, one of which is the underlying cause of the dielectric failure.

As shown in Figure 2.13, there is a relationship between the strength and duration of the applied electric field that distinguishes different dielectric breakdown mechanisms. The exact shape of the curve is not applicable to all materials; the figure shows a nonspecific example for some material. However, it is helpful in conveying some key information about the associations between the various mechanisms.

Figure 2.13

Breakdown Field Strength vs. Inception Time with Likely Associated Mechanisms

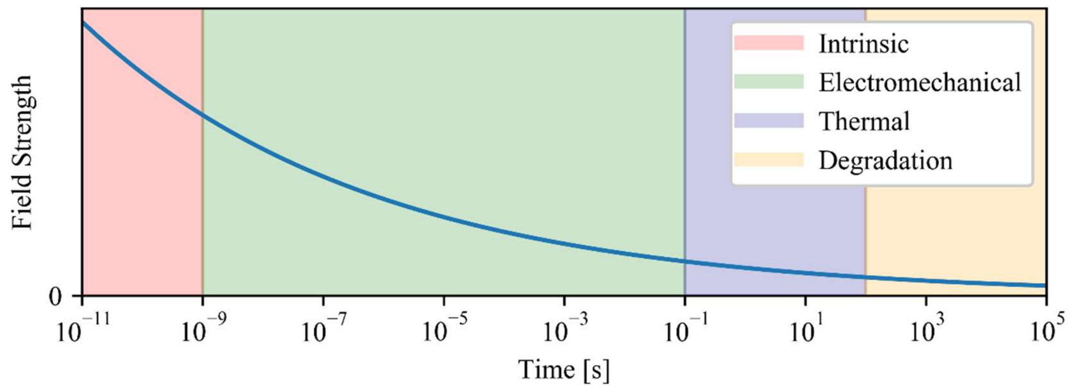

2.4.2.1 Intrinsic Breakdown. In dielectric materials, few electrons are available for conduction, but they can in some circumstances be the sole cause of dielectric breakdown. When in the presence of sufficiently strong electric fields, valence electrons in the dielectric material can be forced into the conduction band. In this time, the electrons can gain high amounts of energy. Other valence electrons which are then crashed into can themselves break free of the valence band and pick up more energy. This process, also known as electronic breakdown, perpetuates through the material, generating heat and damage through the material until a conductive channel has been created. Intrinsic breakdown is named as such because it is a mechanism of breakdown that is not dependent on impurities, mechanical stress, or the surrounding environment, but inherent to the material itself. To measure it requires tightly controlled environmental conditions and a completely homogeneous material without impurities.

2.4.2.2 Electromechanical Breakdown. When opposite charges lie on opposite surfaces of an object of a dielectric material as pictured in Figure 2.14, the attraction

between the two charges apply a compressive mechanical force to that object. If those forces create enough stress to outweigh the compressive strength of the material, the object will fracture. The result is a void which the surrounding gaseous or liquid medium can fill.

Figure 2.14

Breakdown Due to Electrocompressive Forces

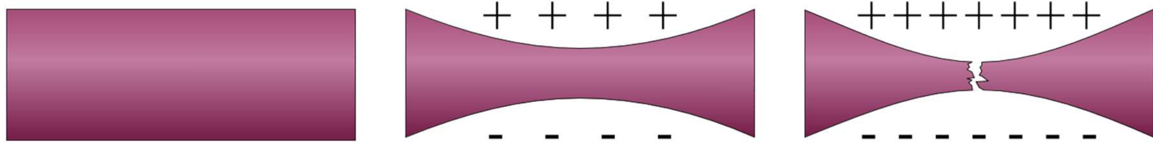

2.4.2.3 Thermal Breakdown. The limited electrical conduction that does occur through a dielectric dissipates energy in the form of heat throughout the material. If the heat being generated is more than the heat dissipated, the temperature of the material can be increased to the point of damage. This damage can either create a void or a channel of altered material, either of which may provide a path for electrical conduction through the dielectric.

2.4.2.4 Degradation (Partial Discharge). An applied dielectric material will typically have considerable defects, voids, and impurities. These features have important consequences which decrease the dielectric withstand capability of the dielectric material. Gas impurities, often having a much lower dielectric strength, are trapped inside the dielectric. Charges accumulate around the impurities in the presence of electric fields and can overwhelm the dielectric withstand capability of the impurity. In this event, a *partial discharge* is triggered through the impurity: a localized dielectric breakdown. While

gaseous dielectrics are unlike solid dielectrics in that they can recover to normal after a discharge event is completed, partial discharges in solids can cause irreparable damage to the material surrounding the impurity. As more partial discharges occur, the likelihood of a conductive channel spanning the thickness of the material or of a dielectric breakdown due to other mechanisms increases.

A simplified model for the system of a dielectric loaded with impurities can be drawn as a series of capacitors, an example of which is shown in Figure 2.15. In this model, a section of the dielectric material between two electrodes is taken. If the section contains no impurities, it can be modeled as a single capacitor: a slice of dielectric material between two conductors. However, a section of the material with a single impurity can be represented by the combination of three capacitors in series. One capacitor spans from the top conductor through the dielectric material to its interface with the impurity, another spans the entire height of the impurity, and a third reaches from the bottom of the impurity to the bottom conductor.

Figure 2.15

Capacitor Model of Dielectric Material Defects

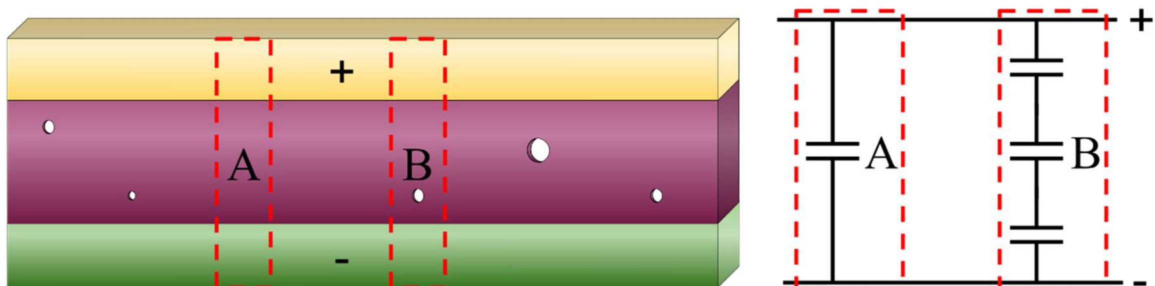

It is important to note the reliance of dielectric strength on the thickness of a material due to partial discharge. For very thin samples, the opportunity for defects to emerge inside their thickness is small, and so the dielectric strength is closer to that of a purely homogeneous material. For a strong dielectric with a higher dielectric withstand capability than the typical contaminant (air, for example), the dielectric strength would measure higher with thinner samples. Thicker samples, on the other hand, have more defects, are more susceptible to partial discharges leading to breakdown, and therefore have lower dielectric strength per unit thickness than thinner samples of the same material.

Partial discharge is typically less of a factor in dielectric breakdown for DC conditions than it is during AC voltage stress. This may be due to the decreased severity and frequency of partial discharges tending to occur in DC-stressed samples relative to that of AC-stressed samples [35].

2.4.3 Breakdown, Sparkover, and Flashover

There is an important distinction to be made regarding the different types of events that can lead to a discharge of potential between two sides of a dielectric. These discharge events are illustrated in Figure 2.16 generally fall into one of three categories: breakdown, *flashover*, and *sparkover*. Breakdown, as illustrated in the previous section, is a discharge through the thickness of the dielectric. That is, a breakdown occurs through the material in the direction perpendicular to the planar surface of the material.

Figure 2.16

Comparison of Breakdown, Flashover, and Sparkover

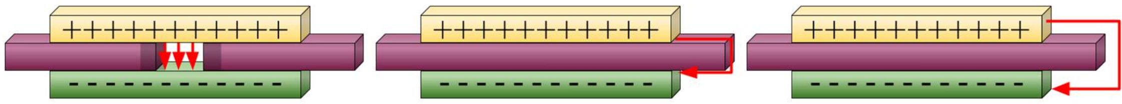

Flashover and sparkover, on the other hand, do not penetrate through the thickness of the material. Instead, the discharge takes a path around the dielectric. If the charge travels through the surrounding medium, the event is classified as a sparkover. However, if it passes along the interface between the surface of the dielectric and the surrounding medium, the event is classified as a flashover. When characterizing a material for its ability to withstand dielectric breakdown, it is critical to minimize the chance for sparkover and flashover, because these events will result in errant measurements that are not representative of the material's properties.

2.4.4 Paschen's Law

Frederich Paschen in 1889 discovered that the breakdown voltage of a gas is dependent on its pressure and on the distance between charged electrodes [36]. He found that the breakdown voltage decreased as the pressure was reduced until a critical pressure was reached. Below this pressure, the breakdown voltage sharply rose, eventually reaching higher than that at atmospheric pressure. With increasing pressures, the breakdown voltage would also increase. This description of the relationship between pressure and breakdown voltage in gases is also applicable in describing the relationship between gap distance and breakdown voltage. Paschen's law, shown as Equation (1) and illustrated for several gases in Figure 2.17, defines this relationship.

$$V_B = \frac{Bpd}{\ln(Apd) - \ln\left[\ln\left(1 + \frac{1}{\gamma_{se}}\right)\right]} \tag{1}$$

Figure 2.17

Paschen's Curve for Various Gases

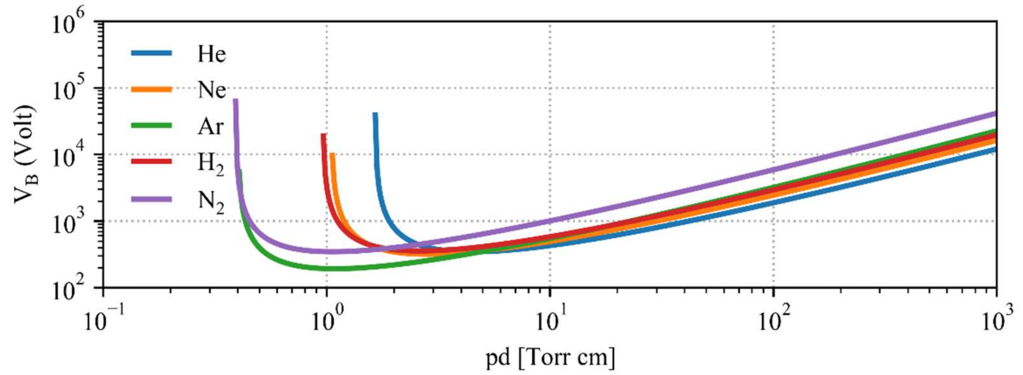

A sufficient understanding of the shape of Paschen's curve requires a more detailed examination of gaseous breakdown. Here, V_B is the breakdown voltage in volts, p is the pressure of the gas measured in pascals, and d is the gap distance in meters. A and B are parameters which are specific to each gas and together define α, the *first Townsend coefficient*. This coefficient describes the mean number of single ionizing collisions per unit length traveled by accelerated free electrons. α can be expressed in terms of A and B as shown in Equation (2) [37, 38].

$$\frac{\alpha}{p} = A\exp\left(\frac{-Bp}{E}\right) \tag{2}$$

With a fixed value of p it is clear that α grows proportionally with A, which would indicate a greater number of ionizing collisions per unit length traveled by a free electron. This increase would logically lead to a decrease in breakdown voltage, and it is clear that this is true when considering an increase in A in Equation (1). Conversely, an increase in B decreases α and thus decreases the mean number of ionizing collisions per unit length. With a lower probability of ionizing events, it is more likely that the gas can support a higher voltage. Again, this logical conclusion is reinforced by the relationship between V_B and B in Equation (1).

γ_{se}, the secondary electron emission coefficient (SEEC) or *second Townsend coefficient*, is the mean number of electrons emitted from a cathode surface following an impact of a single primary charged particle. It depends on the kinetic energy that the particle has gained during its acceleration and on factors such as cathode material and surface quality [39, 40]. Its relationship with incident particle energy is *non-monotonic*, which means that it is increasing and decreasing on different intervals. For many materials, the SEEC is greater than one for some interval of energy, for which it can be expected that multiple secondary electrons may be emitted for each incident particle. This relationship is illustrated in Figure 2.18. If γ_{se} is greater than one, more than one electron is typically emitted for each incident particle making impact.

Figure 2.18

Generic Relationship Between Incident Particle Energy and SEEC

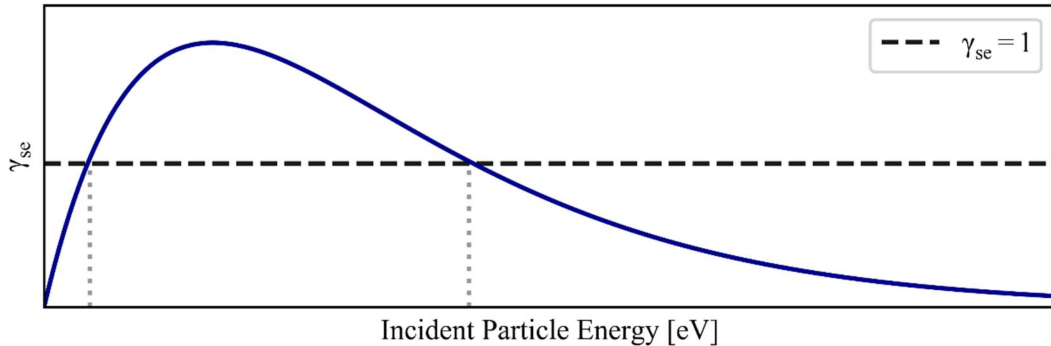

A *Townsend avalanche* is a chain of ionizing collisions (with probability governed by α) between free electrons and gas molecules. A free electron gaining sufficient energy through acceleration in an electric field can release an additional electron belonging to an impacted gas molecule. The newly freed electron now has the potential to accelerate and gain energy itself as it is motivated by the electric field. This electron may also become capable of colliding with another gas molecule and again freeing an additional electron. Further, gas molecules ionized during this process are now affected by the electric field and will begin to accelerate in the direction opposite to that of the electrons. Depending on γ_{se}, more free electrons may be released through secondary emission upon the impact of ions to the electrode surface. The shape of Paschen's curve can now be explained.

The total energy gained by a free electron in a gas as it is accelerated by an electric field is dependent on the gas and its pressure. The mean free path, which is the average distance an atom or molecule can travel before colliding with another, is inherent

to each gas and inversely related to its pressure. In the context of an electron, this is the distance over which the electron can gain or lose energy before a collision occurs. For higher pressure gases, the mean free path is shorter, and there are more frequent collisions. This will limit the kinetic energy gained for an electron because it will change direction upon collisions. For long gap distances, the electric field strength between electrodes will be reduced given the same voltage, and so the acceleration applied to an electron will be reduced. Thus, when the product of pressure and distance is large due to high pressure, long distances, or both, the required voltage for breakdown is high.

On the other hand, when the product of pressure and distance are small, either the pressure is low, the distance between electrodes is short, or both. For low pressures, although free electrons may be able to gain sufficient energy between collisions to ionize gas molecules, the collisions are relatively few and far between. Similarly, short electrode gap distances reduce the chance that an electron collides with a gas molecule before reaching the opposing electrode.

Illustrations of high and low pressure-distance cases can be found in Figure 2.19. In the top left, a high-pressure gas has too many collisions to allow for sufficient acceleration. in the top right, a low-pressure gas sees too few collisions to produce an avalanche. In the bottom left, the mean free path between molecules might allow sufficient acceleration, but the electric field strength is diminished due to the extended electrode gap length. Finally, in the bottom right image, the gap distance is too short to allow enough acceleration or collisions before an electron would reach the opposing electrode.

Figure 2.19

Effects of Pressure and Gap Distance on Free Electron Collisions

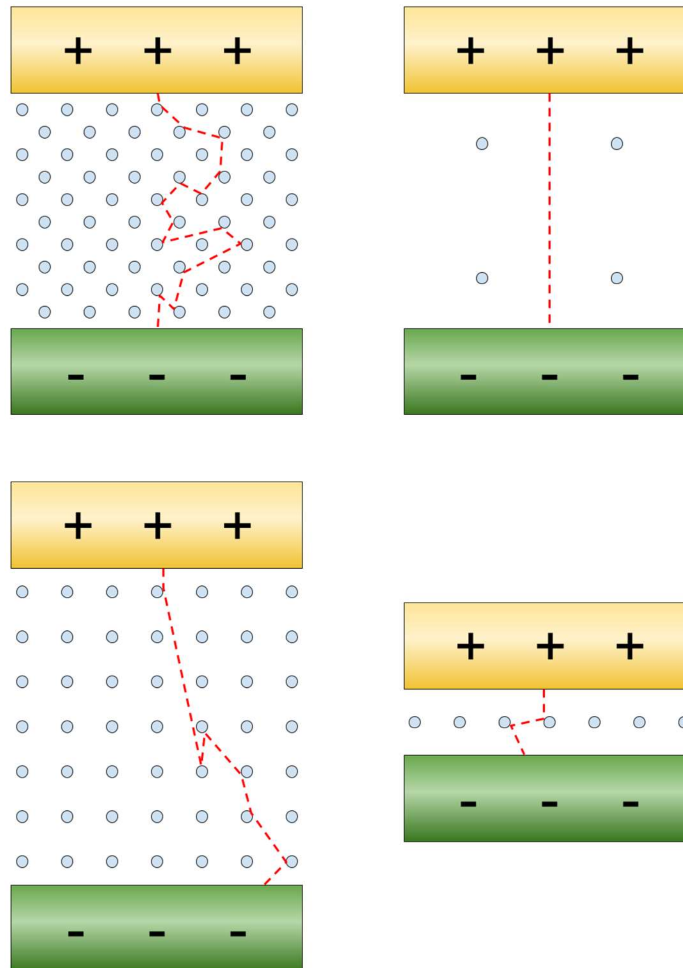

There exists a minimum breakdown voltage for any gas between these high and low cases for pressure-distance. This voltage, known as the *Paschen minimum*, can be found by differentiating Equation (1) with respect to pressure-distance and setting the result equal to zero. By solving the resulting equation for pressure-distance, the minimum breakdown voltage and the pressure-distance needed to achieve it for a gas can be found, assuming that the relevant coefficients have been determined.

It is important to understand Paschen's law when collecting dielectric strength data. For dielectrics that can withstand strong electric fields, the dielectric strength of the surrounding medium can be an issue due to the possibility that it may break down before the dielectric under test. The probability for a sparkover event is affected by the breakdown voltage of the gas, which is a function of Paschen's curve. For example, reducing the pressure of the gaseous medium in a dielectric test system could increase the chance for sparkover, which could be incorrectly detected as a breakdown by a test system. Awareness of where the test system's circumstances fall on Paschen's curve can help reduce errant measurements and wasted time or resources.

2.4.5 The Weibull Distribution

For some cases, the dielectric strength data captured in this work and some referenced works are fit to a Weibull distribution. The Weibull distribution is useful for describing random variables associated with lifespan of parts and failure withstand capability. Its cumulative density function (CDF) is especially elucidating for the probability of failure against stress or for predicting lifespans of parts:

$$F(x) = 1 - \exp\left(-\left(\frac{x - \theta}{\alpha}\right)^{\beta}\right) \tag{3}$$

Equation (3) is the CDF for a 3-parameter Weibull distribution [41]. Here, x is a random independent variable, and $F(x)$ is the probability for failure resulting from the conditions of x. For example, x could be a duration of use, and $F(x)$ could be the chance that a bearing in some machine will fail by that time. The scale parameter, α, is also known as the *characteristic life* and coincides with the value of x that results in a 63.2%

chance of failure. β is the curve's shape parameter, otherwise called the *Weibull slope*. The Weibull slope describes whether failures are more probable at the beginning or end of life. If β is less than one, failures occur earlier, if it is one, they are most uniformly distributed for the entire span of x, and if it is greater than one, failures are more likely to occur after some time. Finally, a location parameter, θ, shifts the whole curve to the left or right. As B approaches infinity, the CDF converges to a vertical line at the scale parameter plus the location parameter, indicating that all failures occur precisely at $\alpha+\theta$. Figure 2.20 shows an example of a Weibull CDF with α = 100, θ = 25, and various values of β.

Figure 2.20

Cumulative Density Function for Nonspecific Weibull Distribution

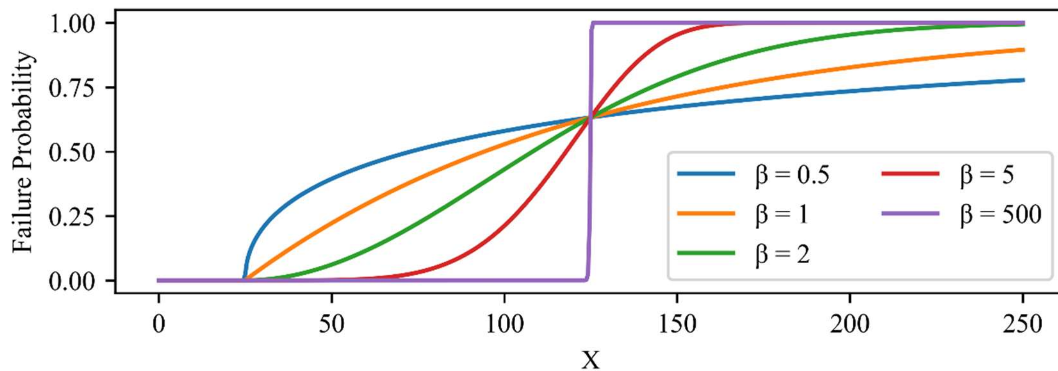

For this work, the Weibull distribution can be used to generalize the likelihood of dielectric breakdown in the presence of electric fields. The random variable x in these cases will be represented by the strength of an electric field across a sample. There are two piece of information that can be easily extracted when comparing Weibull

distributions. First, the left-to-right position of the curve gives an indication of its general robustness. Moving a curve to the left would suggest that it is weaker, whereas moving it to the right would suggest that it is stronger. Second, the slope of the curve is associated with the spread in the data. If it is very horizontal, there is high variability in the data. If it is very vertical, the variability in the data is limited, and any data point is more likely to be near the characteristic life of the Weibull distribution.

2.5 Nanocomposites

2.5.1 Overview

Composite materials combine two or more materials in such a way that maintains discrete phases between each. That is, they do not become new homogeneous materials due to molecular bonds. Instead, the identities of the composite material's components are preserved, although their combination acts as a singular volume. Examples of composite materials include concrete, plywood, and Formica.

Components of composite materials fall into one of two main categories: matrix (host-matrix, binder) and filler (reinforcement). The matrix serves as a host for the filler, binding it together and providing physical structure. Fillers are added to the host in some concentration, and as a result have some effect on the properties of the host matrix. For example, the addition of a filler of aggregate to a cement matrix forms concrete—a composite that is stronger and more durable than the host cement by itself.

Nanocomposites are a subset of composite materials in which the filler material consists of particles or aggregates which are sized 100 nm or smaller in at least one dimension. The tiny size of filler materials in nanocomposites provides advantages to the

physical properties of the composite. For example, crystalline silica is a rigid material with a low CTE. If silica aggregates of microscale or greater are introduced to a flexible host with a relatively high CTE, the mismatches in these properties between the matrix and filler materials can cause mechanical stresses which ultimately lead to failure. However, nanoscale particles have a much higher ratio of surface area to interior volume, and so a higher percentage of the filler material shares a boundary with the host matrix. Stresses due to mechanical property mismatches are in this case distributed more evenly in the composite, rather than highly concentrated at the microscale. This allows the filler material to provide property enhancement similarly to macro-scale composites, but without some of their considerable adverse effects. This result is well known as a key benefit to the use of nanocomposites.

2.5.2 Tuning the Coefficient of Thermal Expansion with Nanoparticles

The high-level objective of this work is to create a flexible dielectric with a strong capability for withstanding electric fields and a coefficient of thermal expansion which is matched to that of copper. Since the addition of a filler to a host matrix can alter its properties, and since maintaining a nanoscale particle size for the filler material can mitigate adverse mechanical effects of composite generation, it may be possible to use a nanofiller to tune the CTE of a matrix and create a useful material that meets the expansion criteria.

The material components of these nanocomposites would consist of materials that have CTE values surrounding that of the target CTE. For example, a polymer matrix with a greater-than-desired CTE would require a filler material with a CTE lower than that of the target. By controlling the weight percent of filler in the composite, the CTE can be

adjusted as called for by the application. Other properties of concern include flexibility of the host matrix, dielectric strength, availability, and readiness for nanocomposite incorporation. For these reasons which are expanded on in the next sections, polyimide (PI) and silica (SiO_2) are matrix and filler material candidates.

2.6 Polyimide/Silica Nanocomposites

In recent decades, Polyimide/silica nanocomposites are commonly selected for suitability analysis in a variety of applications. To understand why, it is important to first examine their components. As CTE is ultimately the target for optimization, it is essential to be aware of the CTE for these materials and how they relate to that of copper. Figure 2.21 shows empirical data for contraction at cryogenic temperatures of the chosen materials of interest to this work [42]. This data provides necessary context for the selection of nanofiller concentrations for examination.

Figure 2.21

Thermal Contraction in Polyimide, Silica Glass, and Copper at Low Temperatures

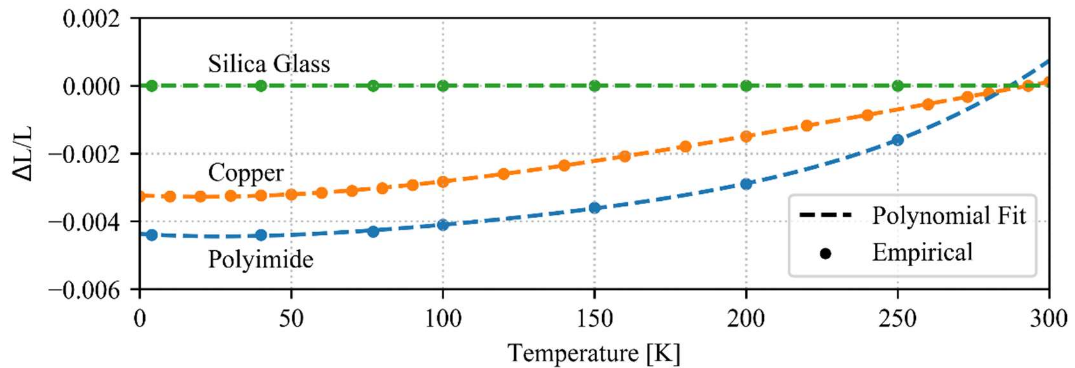

2.6.1 Polyimide

Aromatic polyimide (PI) is an easily obtainable, widely applied organic polymer. It's electrical, mechanical, and chemical properties make the material a very common tool in electronics, aerospace, and other industries. Its ubiquity is due in part to DuPont's Kapton product, select properties of which are highlighted in Table 2.1.

Table 2.1

Properties from Kapton HN Datasheet.

Property	Value	Unit	Condition
Tensile Strength	231	MPa	@23°C
Coefficient of Thermal Expansion	20	ppm/°C	—
Dielectric Strength	303	kV/mm	—

The low cost of entry into PI synthesis makes it an even more attractive option for customization through the integration of nanoparticles. PI can be produced through a thermal imidization reaction of polyamic acid (PAA). In addition, there is potential for UV curing of PAA into PI for applications which may limit the maximum allowable curing temperature. PAA, a viscous liquid at room temperature, can be heated to remove water and solvents in order to produce PI easily and cost effectively. This imidization reaction, pictured in Figure 2.22, can be evaluated by the percent of lost solvent mass, with percent losses of water in the high 90s considered sufficiently imidized [43].

Figure 2.22

Imidization with Atoms Removed During Reaction Highlighted

Polyamic acid

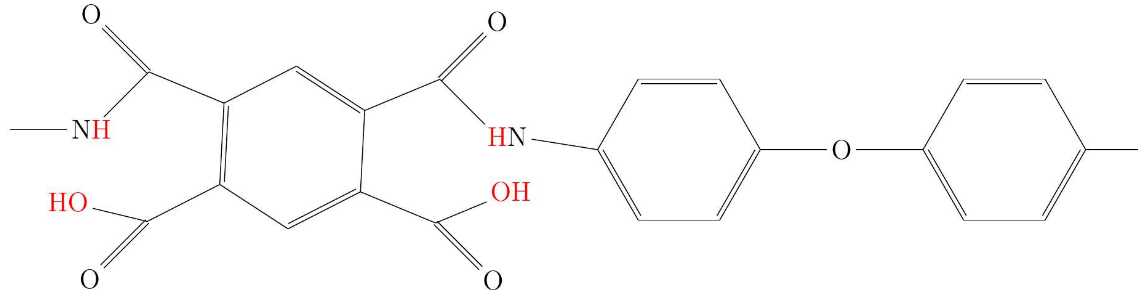

↓↓ Thermal imidization (-2nH_2O) ↓↓

Polyimide

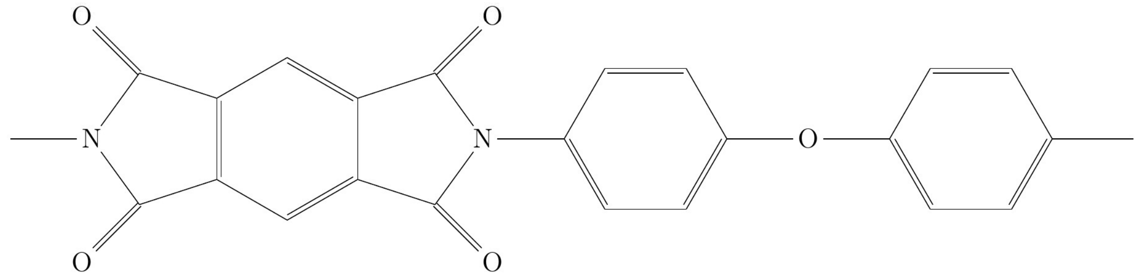

Nanoparticles can be introduced into PAA and then solidified into the resulting PI after imidization through either *in situ* or *ex situ* processes. For the in situ case, filler material is generated inside the matrix material after its constituents are introduced through a precursor solution. Ex situ processes, on the other hand, are performed through the direct addition of existing filler particles into the host material.

2.6.2 Silica

Silicon dioxide is a ubiquitous oxide of silicon that is found in many forms and has a wide variety of applications. For example, it can be found in an amorphous form as fused silica glass; in several crystalline forms; and as silica gel, a common desiccant.

Silica is electrically insulating, brittle, has a high melting point, and, importantly to this work, is very resistant to changes in size due to heating and cooling. As shown in Table 2.2, SiO_2 has a lower dielectric strength compared to polyimide, but its CTE is much lower [42, 44]. Although silica may be more brittle and electrically weaker, its properties make it a good candidate for a filler material in a polyimide matrix in this application.

Table 2.2

Select Properties of Silicon Dioxide

Property	Value	Unit	Condition
Tensile Strength	110	MPa	@24°C
Coefficient of Thermal Expansion	0.4	ppm/°C	—
Dielectric Strength	15-25	kV/mm	—

Generating in situ silica nanoparticles in polymer matrices can be accomplished through a *Stöber process* [45]. In this technique, DI water, ethyl alcohol, hydrogen chloride, and tetraethyl orthosilicate (TEOS), are mixed together to form a silica precursor solution. After introducing the solution to the host matrix and through stirring, silica nanoparticles precipitate from the TEOS and form spherical particles. The size, concentration, and dispersion of the particles can be tuned through the adjustment of ratios between the precursor components and other process refinements.

2.7 Relevant Previous Works

There have been many previous works examining the properties of nanocomposites and how they are affected by the addition of filler materials. This section reviews some of those that relate to the dielectric strength and mechanisms of breakdown for PI/SiO_2 and other nanocomposites at room and low temperatures.

2.7.1 Electric Field Enhancement with Composite Filler Addition

As discussed in Section 2.4.2, partial discharges occurring throughout the volume of an electrically stressed nanocomposite material are a common cause of dielectric breakdown. In 2004, Nelson and Fothergill demonstrated the localized enhancement of electric fields in epoxy-based composites with particle size regimes of nano and micro scales [46]. Titanium dioxide (TiO_2) nano particles were incorporated into an epoxy host matrix with a nominal concentration of 10%. The particle sizes were controlled to fit into one of two regimes with 23 and 1500 nm average particle sizes.

A pulsed electro-acoustic system was used to measure the charge distribution throughout the length of samples in response to applied electric fields of 3 kV/mm RMS. A simplified model of a pulsed electro-acoustic (PEA) measurement system is shown in Figure 2.23 [47]. In this method, a dielectric is first subjected to a sustained high voltage. The electric field eventually leads to a steady state charge distribution throughout the dielectric in which defects and other material discontinuities produce non-uniformity. With this steady state reached, a short (nanoseconds) voltage pulse is then introduced to the positive electrode. The voltage strengthens the electric field for a moment in which the concentrations of charge throughout the dielectric are subjected to a force. Although the effect of the electric field effects the entire dielectric virtually in one instant, there is a pressure wave generated for each concentration of charge which propagates at a much slower rate. A piezoelectric sensor on the opposite side of the negative electrode receives these pressure waves and generates an output which can be read on an oscilloscope. Each voltage spike on the oscilloscope signal is proportional to an associated charge concentration. The first spike to appear is generated by the charge nearest to the negative

electrode (and thus the piezoelectric sensor), and the last one to appear is generated by the charge nearest to the positive electrode.

Figure 2.23

Model of a PEA System for Measuring Dielectric Space Charge Distribution

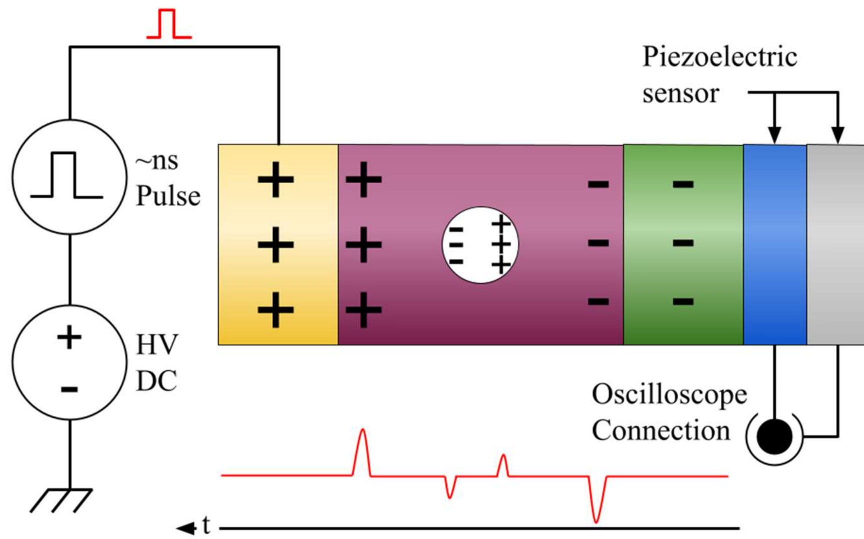

For Nelson et al., PEA results were used to extract charge and electric field distribution data which was compared for the large and small particle composite regimes. Over time, as shown in Figure 2.24, the maximum electric field enhancement was greater for the microcomposite samples than it was for the nanocomposite samples.

Figure 2.24

Electric Field Strength in Epoxy/TiO_2 Composite Samples

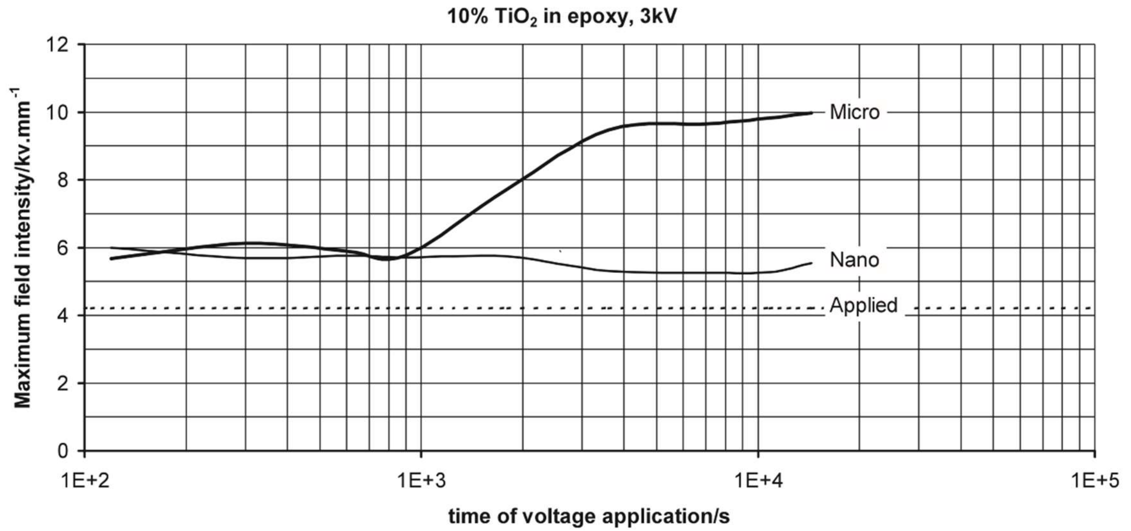

This work also included dielectric strength measurements, the results of which further illustrate the relationship between particle size, localized electric fields, partial discharge, and dielectric withstand capability. The same two regimes of TiO_2 composite materials were produced with filler concentrations between 1% and 40%. Dielectric strength measurements were made with ramping DC voltage stresses of 500 V/s. There are two clear outcomes of the tests. First, higher particle concentrations resulted in decreased dielectric withstand capability. Second, the composites with larger particles consistently had lower dielectric strength for all concentrations. These results can be seen in Figure 2.25.

Figure 2.25

Dielectric Strength of Epoxy/TiO_2 Nano/Micro (a/b) Composites

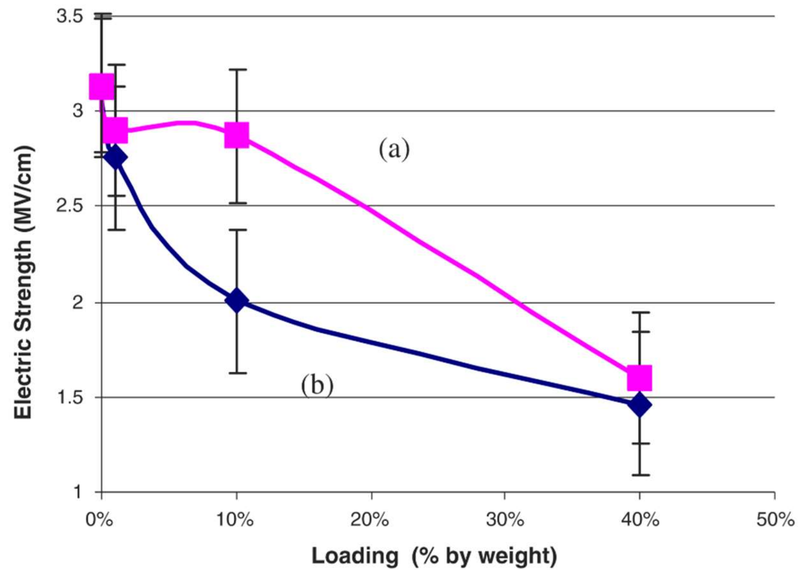

2.7.2 Dielectric Strength of Epoxy/TiO_2 Nanocomposites at LN Temperatures

Another study of epoxy/TiO_2 nanocomposites, published in 2010, characterized the dielectric strength of its specimens at LN temperatures [48]. Nanocomposite films consisting of a cryogenic epoxy (Araldite 5808) loaded to 2.5% concentration with TiO_2 particles sized 5 nm or less were produced through an in situ process. At 77 K the films were subjected to a ramping 60 Hz AC electrical stress with an amplitude rate of rise of 500 V/s to the point of dielectric breakdown. The results of the composite films as well as those for pure epoxy can be seen in Figure 2.26. Here, it is important to note that the dielectric strength of titanium dioxide is 4 kV/mm—approximately an order of magnitude lower than that of the host matrix. Despite this, the data suggest a 56% increase in dielectric strength at 77 K after the incorporation of the nanoparticles. The authors

attribute the improved performance to decreased polymer chain mobility caused by the introduction of nanoparticles.

Figure 2.26

Dielectric Strength of Epoxy/TiO_2 Composites and Pure Epoxy at 77 K

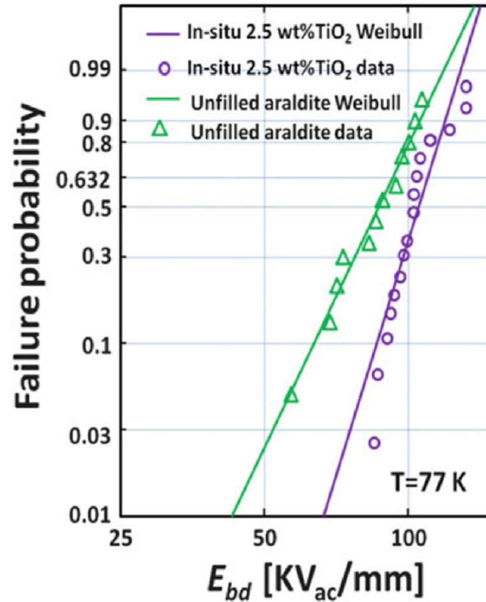

2.7.3 Effects of Particle Dispersion on Dielectric Withstand Capability

Polyethylene (PE)/montmorillonite (MMT) nanocomposites of 5% filler concentration were produced by Vaughan et al. in 2006. While maintaining the 5% nanoclay filler concentration, the filler dispersion was adjusted through the selection of composite generation methods. Films of 53 μm thickness immersed in silicone oil were tested for their dielectric strength with the application of a 50 V/s ramping 60 Hz electrical stress. The Weibull distribution of the results can be found in Figure 2.27. These results show that the dielectric strength of the composite material is dependent on the effectiveness of the nanoparticle incorporation method and of the presence of larger

agglomerates in the material. Specifically, better uniformity of the particle distribution through the material leads to improved dielectric strength. In addition, the samples with better dispersion also had less variance in their breakdown measurements, as suggested by the steeper slope present in the Weibull data on the right of the Figure.

Figure 2.27

Dielectric Strength vs. Dispersion Quality in PE/MMT Nanocomposites

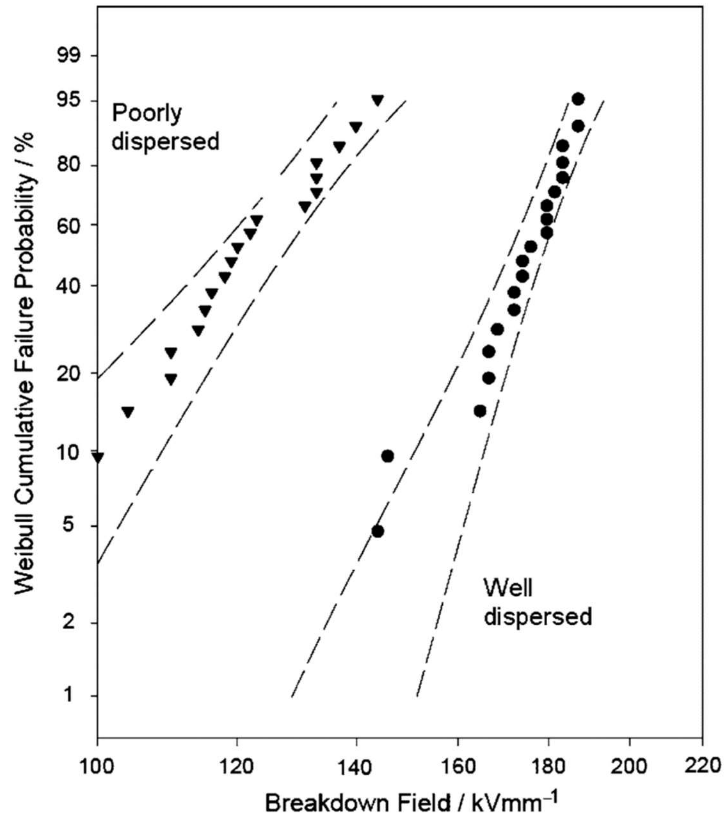

2.7.4 Room Temperature Dielectric Strength vs. Filler Concentration in PI/SiO_2 Nanocomposites

Cui et al., in 2015, generated in situ PI/SiO_2 nanocomposite films of filler concentrations ranging between pure PI and 10% wt. silica [49]. Particle sizes between

10 and 30 nm were reported. The results of dielectric breakdown tests, as seen in Figure 2.28 indicated a slight increase in dielectric strength with low concentrations of silica. With filler concentrations greater than 4%, however, the dielectric strength decreased. It may be noteworthy, however, that this work reports a significantly lower dielectric strength of pure PI than do most other works.

Figure 2.28

Dielectric Strength vs. Filler Concentration in PI/SiO₂ Nanocomposites

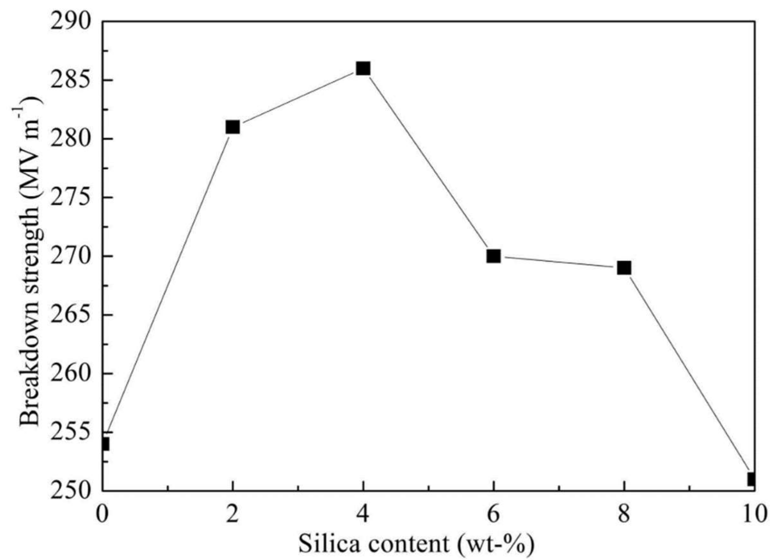

Another study by Weng et al. in 2017 measured mechanical and dielectric properties of PI/SiO_2 nanocomposites for various silica concentrations [25]. The results of the experiment are included in Table 2.3. In this work, the dielectric strength was lowest for pure PI, and increased with higher filler loading.

Table 2.3

Dielectric Strength of PI/SiO_2 Nanocomposites vs. Silica Concentration.

Material	Dielectric Strength [kV/mm]
Pure PI	160.2
4% SiO_2	214.0
8% SiO_2	218.3
12% SiO_2	229.8
16% SiO_2	288.8

While illuminating in some respects, the two works described in this section leave some uncertainty regarding the investigation of PI/SiO_2 nanocomposite dielectric strength. It is particularly unclear how to compare these results with any other, due to the absence of any film thickness data in the reports. As described in Section 2.4.2, the thickness of the film under test is a vital consideration to make due to the increased likelihood of voids and other defects which cause decreased dielectric strength in thicker samples. Without this information, it is not clear how representative these measurements are to the inherent properties of the material, or if they are significantly skewed by impurities.

2.7.5 Cryogenic Dielectric Strength of Polyimide

Experiments on the dielectric breakdown of polyimide films at cryogenic temperatures resulted in a negative correlation between temperature below 300 K and dielectric strength. In this study, published as part of the conference proceedings of the Asia-Pacific Power and Energy Engineering, a pair of opposing cylindrical electrodes was installed into a cryogenic vacuum chamber [50]. Polyimide films of 25 and 50 μm thicknesses were generated. A ramping voltage of 500 V/s was applied across a

polyimide film sample between the electrodes. Measurements were taken at 25 K steps between 300 K and 78 K.

The results of this work showed a clear increase in dielectric strength for all films as temperature decreased. The peak gain in dielectric strength at 78 K was almost 24%. In addition, the thinner 25 micrometer sample saw a more significant improvement at lower temperatures than did the thicker samples.

Decades earlier, similar work tested the dielectric strength of various polymers such as polyimide under a number of conditions [51]. The polymers—films of 50 micrometer thickness—were submerged in silicone fluid at room temperature, liquid nitrogen, liquid helium at 5 K, and held in a vacuum at 5 K. Dielectric strength measurements were taken in each of the conditions. The results indicated that polyimide became electrically stronger in all low temperature environments. It is not possible, however, to make direct comparisons between the two studies in this section, despite their similarity, because of the differing mediums in which the tests were performed. The results from both studies are shown in Figure 2.29.

Figure 2.29

PI Dielectric Strength at Temperatures Between 5 K and Room Temperature

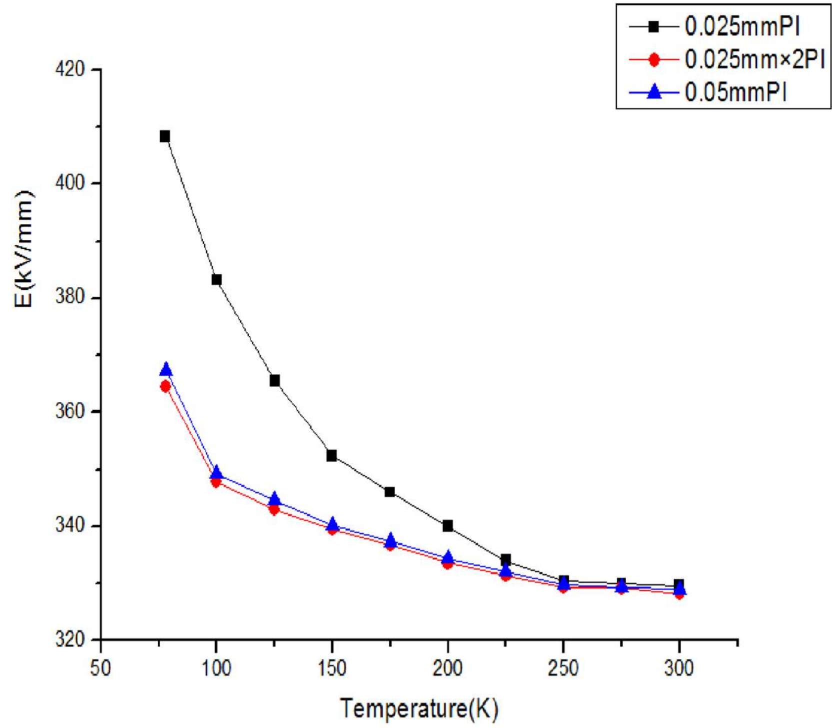

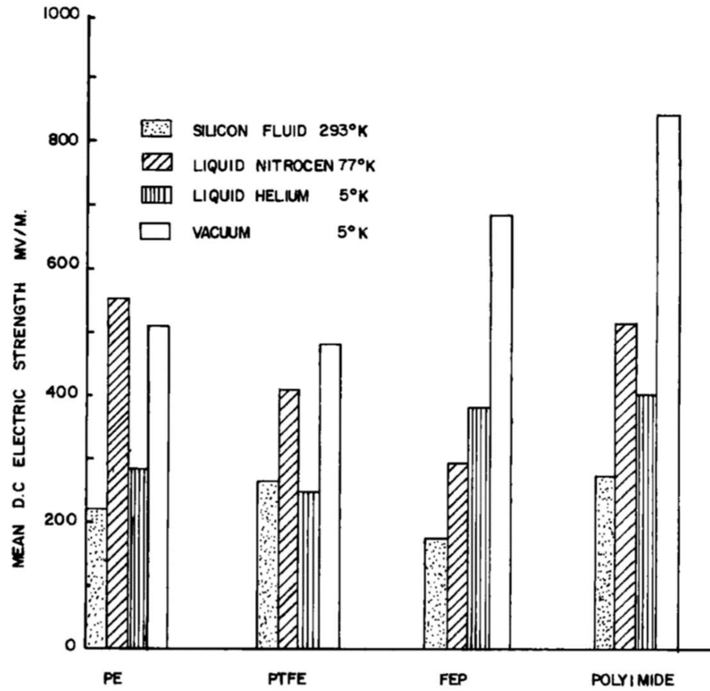

2.7.6 Cryogenic CTE vs. Filler Concentration in PI/SiO_2 Nanocomposites at Low Temperatures

A team of researchers at the Shenyang National Laboratory for Materials Science published work in 2006 that examined the thermal expansion of PI/SiO_2 nanocomposites between temperatures of 153 and 473 K. Nanocomposites with filler concentrations of 0-15% were produced with an in situ method. The material was cast into films of 50 micrometer thickness and mounted into an optical thermal expansion measurement system. The system was subjected to the target temperatures and its size was measured with optical edge detection.

The results of the study show that the particle addition had a notable effect on the CTE of the film. The films with higher concentrations had a much lower change in size at low temperatures than did those with lower nanofiller loading. The result which can be seen in Figure 2.30 may suggest promise for the high-level target of the films in this paper: a nanocomposite dielectric with a CTE matching that of copper.

Figure 2.30

CTE vs. Temperature and Filler Concentration for PI/SiO₂ Nanocomposites

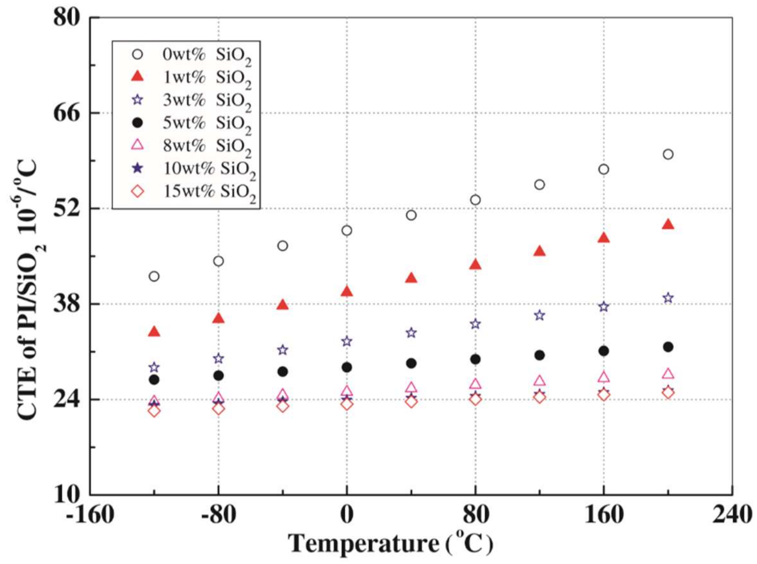

Chapter 3

Experimental Methods

The sections in this chapter describe the methods used to collect room temperature and cryogenic dielectric strength measurement data for polyimide/silica nanocomposites. Preparation and verification of samples, room temperature dielectric test system design, low temperature dielectric test system design, test procedures, and failure analysis procedures will be discussed.

3.1 Sample Preparation and Verification

3.1.1 Film Preparation

Silica particles were generated in a sol-gel created through the Stöber process with a solution of the materials shown in Table 3.1 [45]. The solution was mixed at 50 RPM for 30 minutes, creating a sol-gel through the Stöber process. The sol-gel was then added to PAA solution, the amount of which is determined according to the desired resulting weight percent of silica in the composite and the following equation.

$$n = \frac{m_{silica}}{m_{silica} + m_{PI}} = \frac{C_1 m_{sol-gel}}{C_1 m_{sol-gel} + C_2 m_{PAA}} \tag{4}$$

Table 3.1

Materials Required for Silica Sol-Gel

Material	Weight Percent
Water	5.8
Ethyl alcohol	14.9
Tetraethyl orthosilicate (TEOS)	67.5
Hydrochloric acid	11.8

In Equation (4), the expected ratio of silica mass (m_{silica}) to total nanocomposite mass ($m_{silica} + m_{PI}$) is equal to the ratio of the expected yield of silica ($C_1 m_{sol}$) from the sol-gel to the sum of it and the expected yield of PI from PAA after imidization ($C_1 m_{sol-g} + C_2 m_{PAA}$). The constants C_1 and C_2 represent the percent yields for the sol-gel (to silica) and the PAA (to PI), respectively. To determine C_1 and C_2, sol-gel and PAA were cured individually with the same temperature profile to be used when curing the composite films. The individual yield rates of SiO_2 (13.8%) and PI (18.38%) were then used in Equation (4) as their expected yields for the composite [52].

After stirring for 6 hours, the composite solution is ready for forming and imidization. The solution was cast to films via a static spin coating technique, in which a layer of solution is poured onto a 3-by-1 inch glass slide before spinning is initiated. The spin speed profile is shown in Figure 3.1. This profile was chosen to produce films with thickness between 12.5 and 25 µm. Films of these thicknesses were anticipated to breakdown within the limits of the chosen power supply and were thick enough to measure confidently with a handheld digital micrometer.

Figure 3.1

Spin Coating Speed Profile

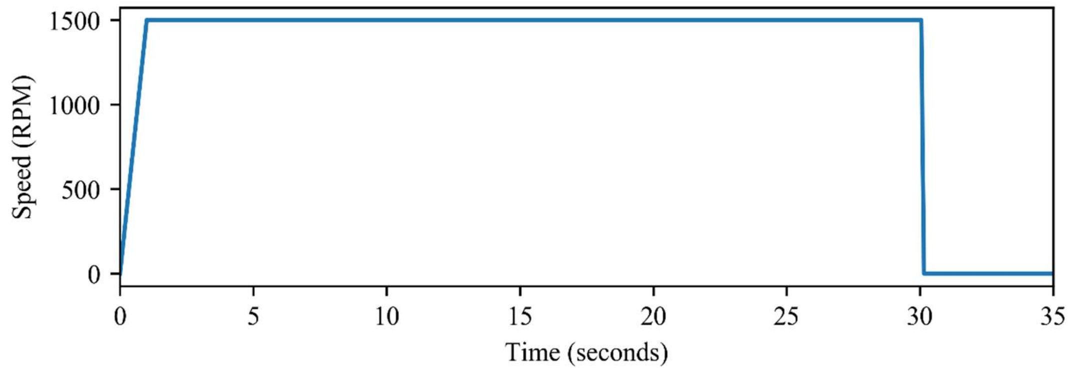

The coated lab slides were then dried on a hot plate. Heat was applied beyond drying at higher temperatures to remove remaining solvents and water and thus complete the imidization reaction. As seen in Figure 3.2, two different curing profiles were used for comparison: one designed to cure but not fully imidize, resulting in a polyamide material, and one which resulted in imidization. The resulting nanocomposite films were stored in a dry and dark cabinet until their characterization.

Figure 3.2

Temperature Profiles for Curing Polyamide and PI Films

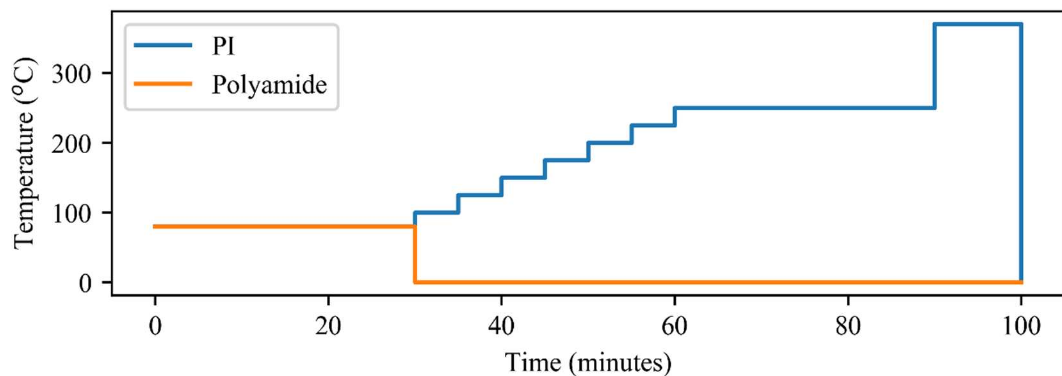

3.1.2 Scanning Electron Microscopy and Particle Analysis

After preparation, the films were subject to scanning electron microscopy in order to verify existence and dispersion of silica particles. Select SEM images were analyzed with computer vision techniques to estimate the particle size distribution. The MATLAB Image Processing Toolbox was used to identify circular objects in SEM images. The radii of recognized circles were returned from the toolbox's *imfindcircles* function [53]. The particles could then be sorted into regimes by their diameter: 0 to 100 nm, 100 to 200 nm, 200 to 300 nm, and so on. This provides insight into the number of particles that fall under the nanoparticle category.

The particle radii were then converted to areas to quantify the pictured surface area of each particle. From this, the diameter regimes can each be characterized for their share of the silica yield in the composite. These data can be used as feedback for improvement of dispersion in subsequent composite samples.

3.2 Room Temperature Dielectric Strength Testing

3.2.1 System Overview

Cylindrical electrodes were machined from stainless steel rods of 6 mm diameter. The edges of one face of each electrode were rounded off, and the opposing ends were turned to 3mm diameter cylindrical tips. The wider, rounded faces are meant for making reliable contact with film specimens, and the narrower ends are sized for easy connection with alligator clips.

The electrodes are embedded into top and bottom halves of an ABS 3D printed fixture with the contact ends of the electrodes facing inward. The bottom half of the

fixture is raised on legs to make clearance for a connection, and the top half is engineered to a mass of 50 grams. A set of rails extending upward from the bottom half act as a guide for the top half, ensuring good alignment between the contact faces of the electrodes. The test fixture is illustrated in Figure 3.3.

Figure 3.3

Room Temperature Dielectric Strength Testing Fixture

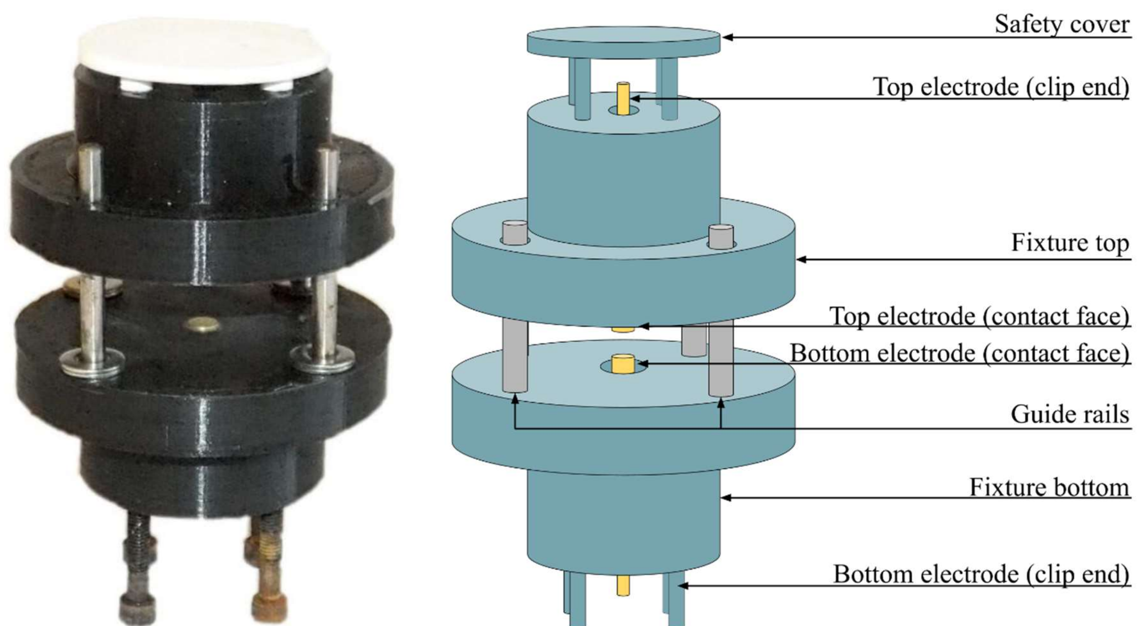

An electrostatic model was built in the ANSYS Maxwell simulation package to gain confidence in the uniformity of the applied electric field. Two electrodes, shaped as described in this section, were arranged such that their wider faces made contact with opposing sides of a polyimide film of 25.4 μm thickness. A 5 kV potential difference excitation was applied to the two electrodes, and a solution was generated by the simulation package. The results of the simulation were used to reinforce expectations that

breakdown events could occur within any point between the contact faces of the electrodes with uniform probability.

A Vitrek 955i high-potential (hipot) safety compliance analyzer (shown in Figure 3.4) supplies the voltage excitation necessary for the test. It's high-voltage and return ports are connected to the top and bottom electrodes, respectively. The device is capable of producing up to 10 kV in AC, DC and pulsed configurations, and can ramp up at various volt-per-second rates. A computer with custom-built software was used to configure tests, run tests, and push data to a cloud database. The computer connects with the hipot tester over an RS-232 connection. Figure 3.5 illustrates the entire system.

Figure 3.4

Vitrek 955i Hipot Tester

Figure 3.5

Room Temperature Dielectric Strength Testing System Diagram

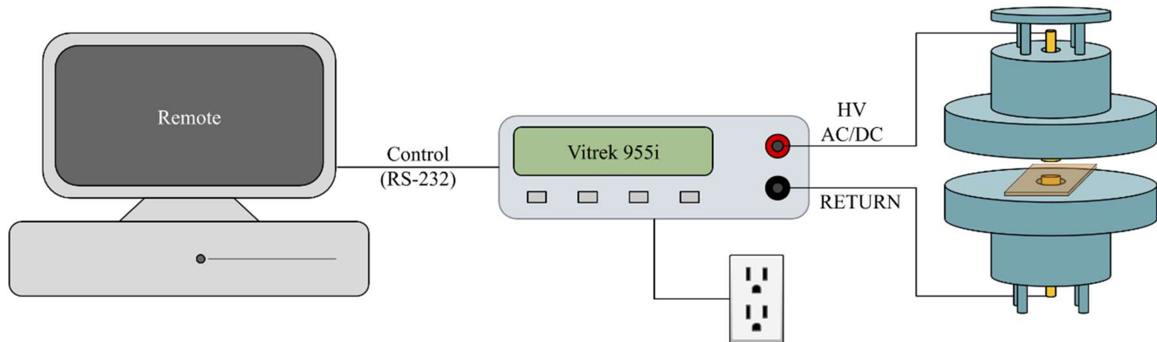

3.2.2 Test Procedure

With all of the system components in place, a sample can be loaded into the test fixture. After careful removal from the slide with a pair of tweezers, a film specimen is sandwiched flatly between the two electrodes, ensuring that 2 mm or more hangs over their edges. The overhanging material is necessary to mitigate the risk of flashover and sparkover. After the sample is loaded, a test can be initiated either through the test automation software or with the manual controls on the hipot tester. The test sequence for this work comprised of a single step: a 500 V/s rate of rise ramping DC voltage until a 5 mA or greater current is detected. With that trip current, the test is ended and the voltage is returned to 0. If the voltage reaches 10 kV and is sustained for 30 seconds with no signs of breakdown, the test is considered passed. Because there is no expectation for the materials under test in this work to be capable of withstanding such stresses, these cases were taken as indicators that the test setup was compromised. For example, the electrodes may require cleaning, or they may not be making adequate contact with the sample. In these instances, the stressed sample was replaced with a new one, the

electrodes were cleaned, and good contact between the electrodes and the sample was ensured.

3.2.2.1 Thickness Measurements. The measurements that are produced by the hipot tester are reported as voltages at the point of breakdown. This is not enough information to make a thorough assessment of the material's dielectric strength. To make this data more useful, it must be normalized according to the thickness of the film. After testing, the samples were measured with a micrometer with a resolution of 1 µm. The thickness measurement is divided into the voltage to find the dielectric strength in units of volts per unit thickness. It is important to measure the thickness of the material only after running a hipot test, not before, because the force of the µm could damage the surface of the film and skew the measurement. Care was also taken to measure the thickness in the same location that the electrodes occupied during the test, to ensure that the measurement is not affected by differences in thickness across the specimen.

3.2.2.2 Control. To ensure that the test system is providing reliable results, it is necessary to take measurements on a known material. Because the host matrix of the material being studied in this work is polyimide, Kapton film was chosen as a readily available and consistent control. According to its datasheet, the expected dielectric strength of 25 µm thick Kapton film is 7.7 kV. Acceptable values were within 10 percent of the datasheet listing. If the results were outside of that window, the electrodes were cleaned, and more care was taken to assert good contact between the electrodes and the next sample. Control measurements were made before running tests on relatively expensive and time-consuming nanocomposite films and regularly when making many measurements in one session.

Figure 3.6 shows a typical test procedure. The electrode configuration, electrode contact force, voltage excitation profile, and thickness measurement comply with the ASTM D3755 standard for dielectric strength testing under direct voltage stress. After testing, samples were verified for breakdown, as opposed to sparkover or flashover, with visual inspection and optical microscopy. The existence of a puncture within the area of electrode contact indicates a dielectric breakdown through the film's thickness. However, signs of discharges other than breakdown were taken as evidence that the electrodes were in need of cleaning, or that they should be making better contact with the sample, or that the sample is too small in the planar dimensions. Typically, discharges around rather than through a sample is marked by a darkened streak extending from the outer circumference of the electrode contact area to the edge of the film.

Figure 3.6

Test Procedure Flow Chart

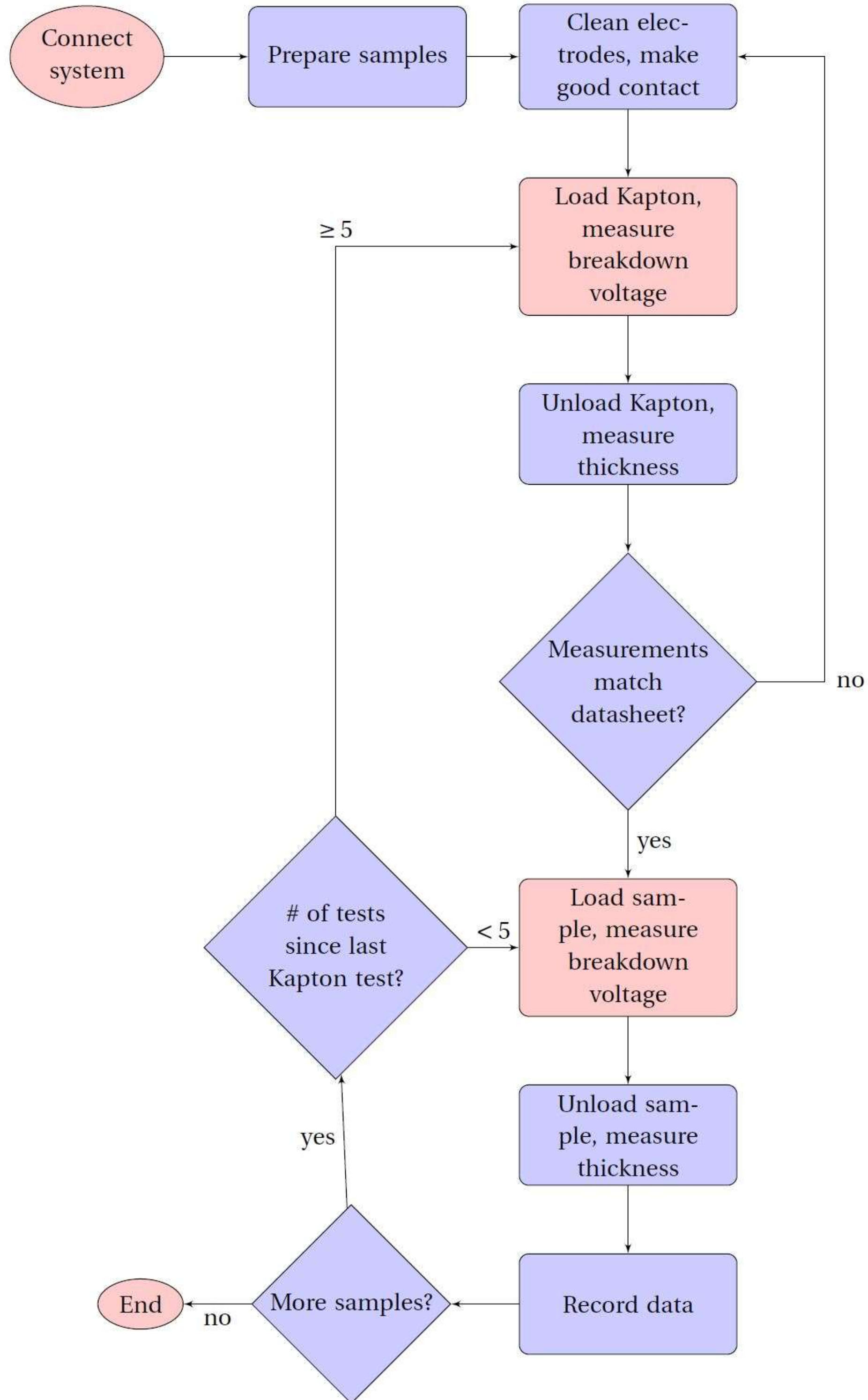

3.2.3 Puncture Verification and Hole Geometry Analysis

To verify the existence of a breakdown event through the thickness of samples and to collect more data regarding the nature of the failures, films were examined under an optical microscope after testing. A Leitz ERGOLUX optical microscope was used to perform this analysis. With an eyepiece magnification of 12.5×, a head magnification of 1.25×, and an objective magnification of 10×, the total magnification of the microscope was 156.25×. This same configuration was used for all microscope analysis, allowing for direct comparison between puncture geometries. These data were examined against SiO_2 concentration, breakdown voltage, sample thickness, and dielectric strength.

3.3 LN-Cooled Testing

Temperatures for GHe-cooled HTS cables can reach much lower than the boiling temperature of LN, but the cryogenic system required to cool helium to those temperatures is time-consuming and expensive to design and build. Also, it can take 5 hours or more to cool the system down for testing, depending on the load. In preparation for future testing in temperatures down to 40 K, it is helpful to make measurements at slightly higher temperatures (referred to as intermediate temperatures onward to avoid confusion) to determine which composites (in terms of nanoparticle concentration) are suitable for GHe testing. For this purpose, a LN-cooled environment was created to run tests at intermediate temperatures. Care was taken to adhere to ASTM D3755 as much as was reasonably possible, but it should be noted that the standard is explicit that its applicable temperature range does not include cryogenics.

3.3.1 Environment

Several attempts were made to design systems which could produce the necessary conditions to obtain dielectric strength data in LN-cooled environments. First, an aluminum chamber was designed and built by a team of engineering students. A photo of the chamber is shown in Figure 3.7. The upper half of the chamber is a small space designed to house a dielectric strength testing apparatus. An aluminum plate separates it and the bottom half of the chamber, which is a vessel for LN. An aluminum rod extending downward into the LN from the separating plate pulls heat from the upper chamber into the LN, which boils away. Ultimately, the design had too many vulnerabilities to outside heat to be effective.

Figure 3.7

LN Testing Chamber Designed for Low-Temperature Measurements

The second attempt at creating a LN-cooled dielectric test consisted of a number of stacked polystyrene cups with a thick foam lid. A dielectric testing rig would be suspended from the inner face of the lid while taking measurements. This design did get down to near 100 K but was not efficient or reliable enough for data collection.

Finally, a test fixture was designed to fit through the neck of a commercial-off-the-shelf LN dewar. The dewar can hold a relatively large amount of LN compared to the previous designs, and is deep and well-insulated enough to reach temperatures near 80 K. It should be noted here that as a consequence of making measurements in an LN-cooled system such as this, the gaseous medium which surrounds the test has changed. For this reason, we cannot directly compare the results of the room-temperature tests, which are surrounded in air, with the low-temperature tests, which occur in a mostly gaseous nitrogen environment. However, it is not unreasonable to use the LN-cooled results as a guide for specimen selection in GHe tests.

3.3.2 LN Test Fixture

A new dielectric strength test fixture was designed to introduce samples into the LN dewar for testing. An array of four electrode pairs, each electrode embedded in a Teflon sleeve, is suspended by a 3D printed mount at the end of a wooden dowel approximately 60 cm long. The electrode pairs are spaced 90 degrees apart around the dowel. Samples were cut to approximately 6x6 mm squares and loaded in between each electrode pair. The electrode pairs were secured together to maintain sufficient pressure for making good contact between them and the samples. Each top electrode is connected to its own 1.63 mm diameter stranded wire. A thinner return wire is connected to all four

bottom electrodes. The supply wire spans the remaining length of the dowel, providing connection points outside the dewar for fast transitioning between tests. A type-K thermocouple (not pictured) accompanies the test fixture and is fixed with Kapton tape at the same height as the sample. An alligator clip lead is connected from the high voltage connection of the hipot tester to one of the top electrode wires, and another secures the return wire to the tester's return port. A photo of the fixture is shown in Figure 3.8.

Figure 3.8

LN-Cooled Testing Fixture for Testing Four Samples at Once

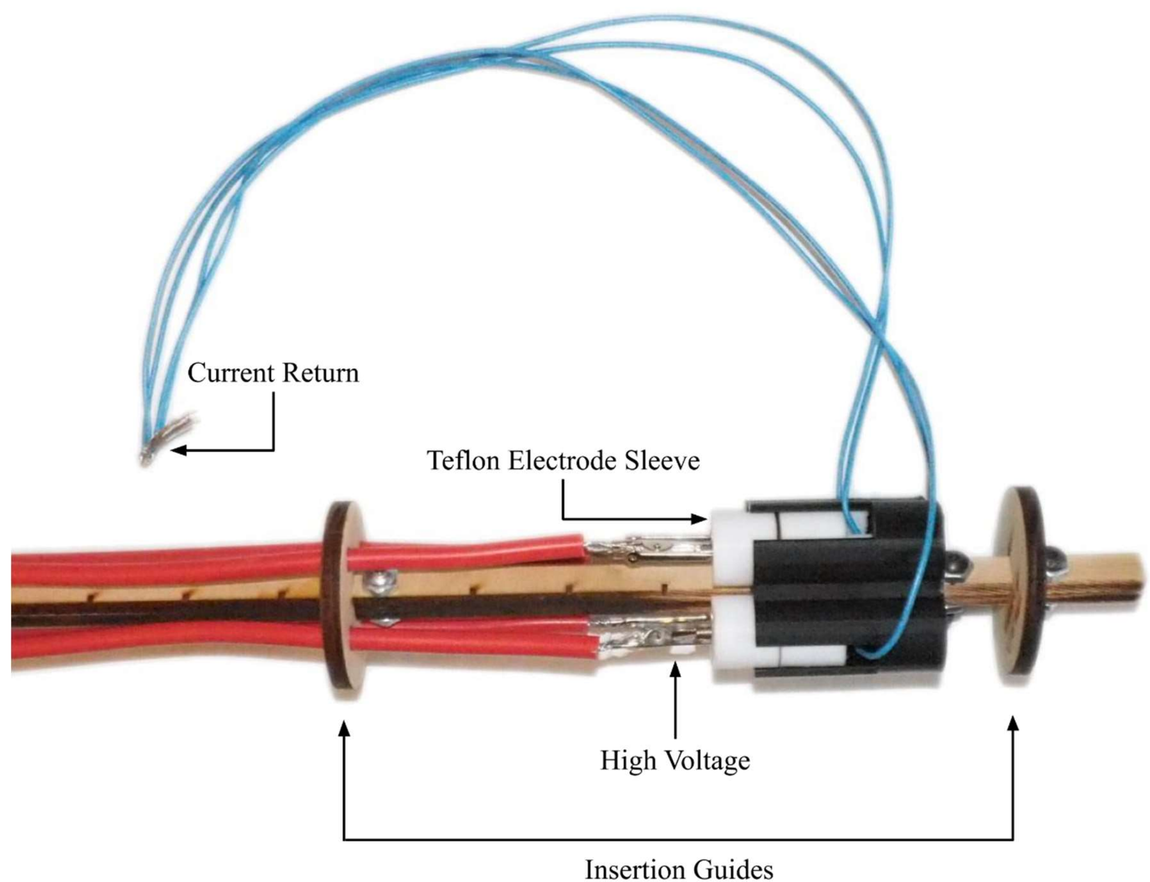

After running a breakdown test, the alligator clip on the top electrode can be simply disconnected and reattached to another yet untested electrode pair. This setup nearly quadruples the productivity of the testing procedure, for which the cool-down process can take 30 minutes or more. In addition to the time required to chill the samples, after testing they must be carefully thawed to make the fixture accessible for sample replacement. A gentle application of heat from a hot air gun sped up this process. Precautions were taken to ensure that the films were not damaged during removal, and that temperatures did not become uncomfortably warm.

Chapter 4

Results and Discussion

4.1 Sample Preparation

Figure 4.1 shows a nanocomposite film occupying a glass lab slide. The films did not vary significantly with color, although the quality of coating did change somewhat depending on the spin-coater operator, the cleanliness of the slide, and the amount of material added to the slide. The surface profile of the films often included edge effects, causing raised outer areas which became lower and more uniform further from the edges. For this reason, samples for testing were generally selected from areas 6 mm away from the sides of the lab slides.

Figure 4.1

Photo of a PI/Silica Nanocomposite Film on a Lab Slide

The thicknesses for the films were collected and plotted in a histogram which is shown in Figure 4.2. All of the films were of thicknesses between 10 and 26 micrometers, with most between 15 and 19 micrometers. The variability of film thicknesses is notable, and is likely due variations in spin-coating and measurement techniques.

Figure 4.2

Thickness Distribution for Room Temperature Test Samples

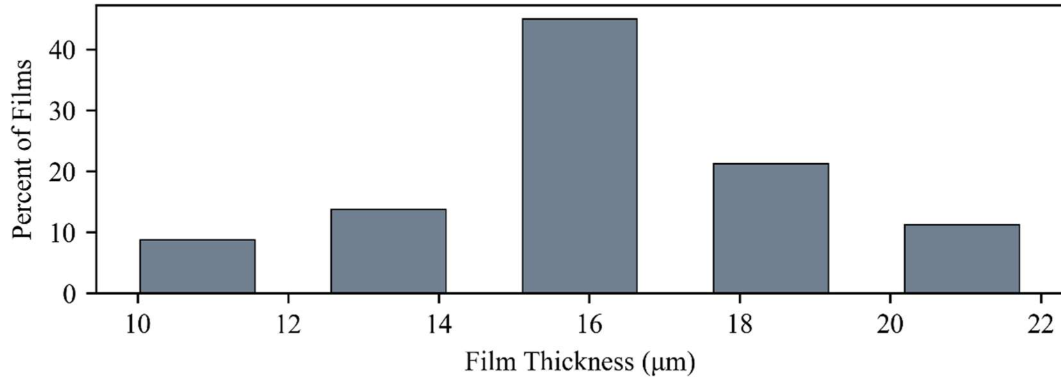

4.1.1 Particle Dispersion

An example of particle detection in SEM images (Figure 4.3) based on circular objects is shown in Figure 4.4. The Image Processing Toolbox functions return the position and estimated radius of all detected objects. With the radius data, some key information can be extracted. The diameter of each circle can be used to estimate the size of its corresponding particle. Although the shape of each agglomerate in the direction perpendicular to the slide is unknown, this analysis can provide an approximation in the other two dimensions. In other words, this data provides an estimate of the number of particles with at least one dimension of sub-100 nm length. This can then be used as feedback for the effectiveness of the material preparation process.

Figure 4.3

SEM Image of Composite Film with 7% SiO_2 *by Weight*

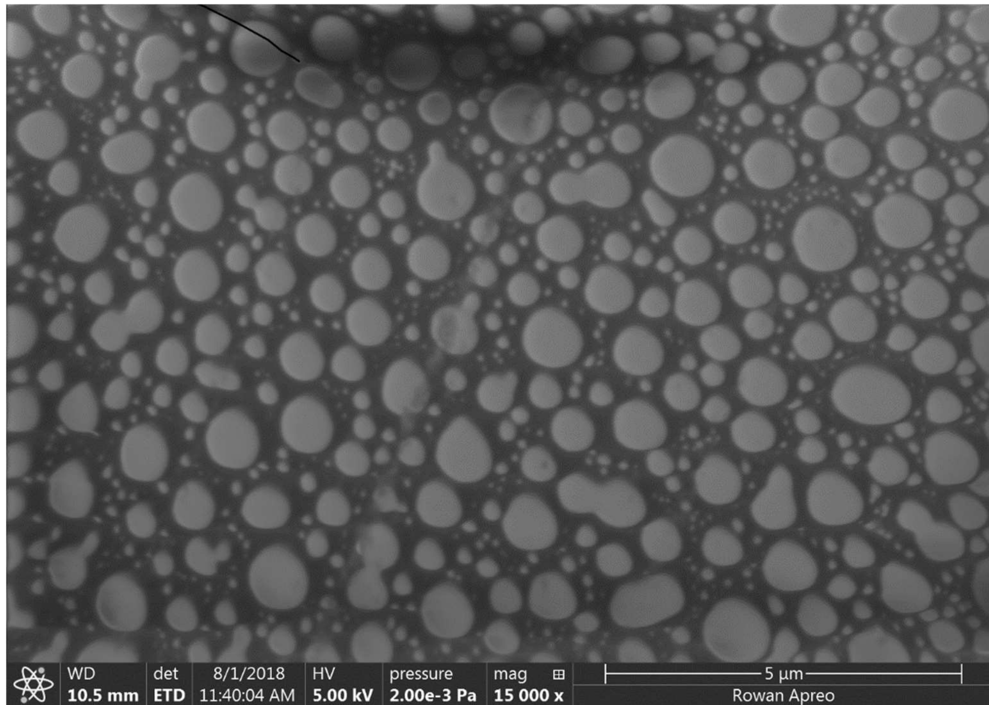

Figure 4.4

Particles Identified with MATLAB's Image Processing Toolbox

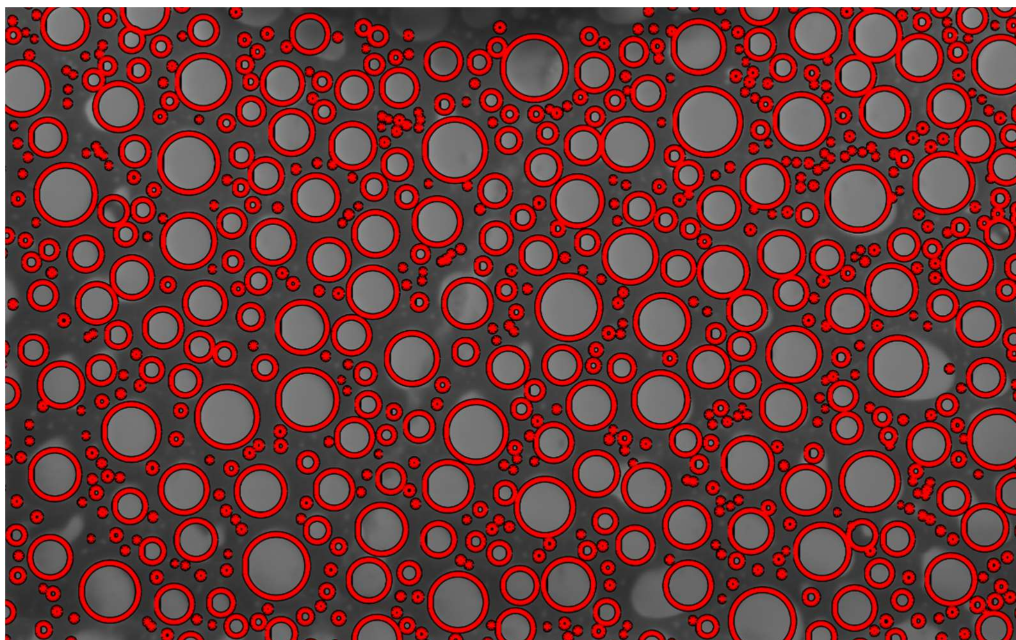

The analysis results shown in Figures Figure 4.5 and Figure 4.6 show how the silica is distributed in the material. Estimates of physical size are obtained by measuring the red circles in pixels and comparing that to the pixel size and physical size of the scale bar. In Figure 4.3, for example, the scale bar represents 5 μm and is approximately 550 pixels long in the image format provided by the microscope. So, for this image, any measurement in pixels can be converted to an estimate in μm by multiplying the pixel value by the scale bar's ratio of μm to pixels.

Figure 4.5

Particle Count in Each Size Regime Among Particles Circled in Figure 4.4

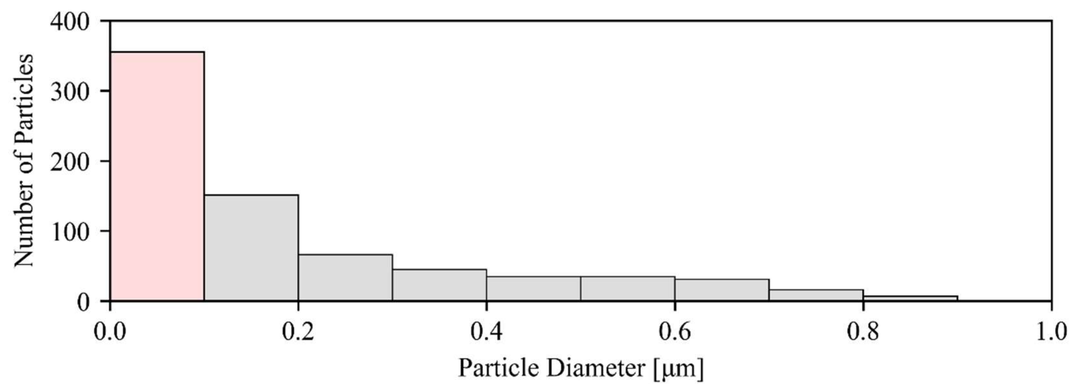

Figure 4.6

Distribution of Silica Pixels in Figure 4.3 Among Particle Size Regimes

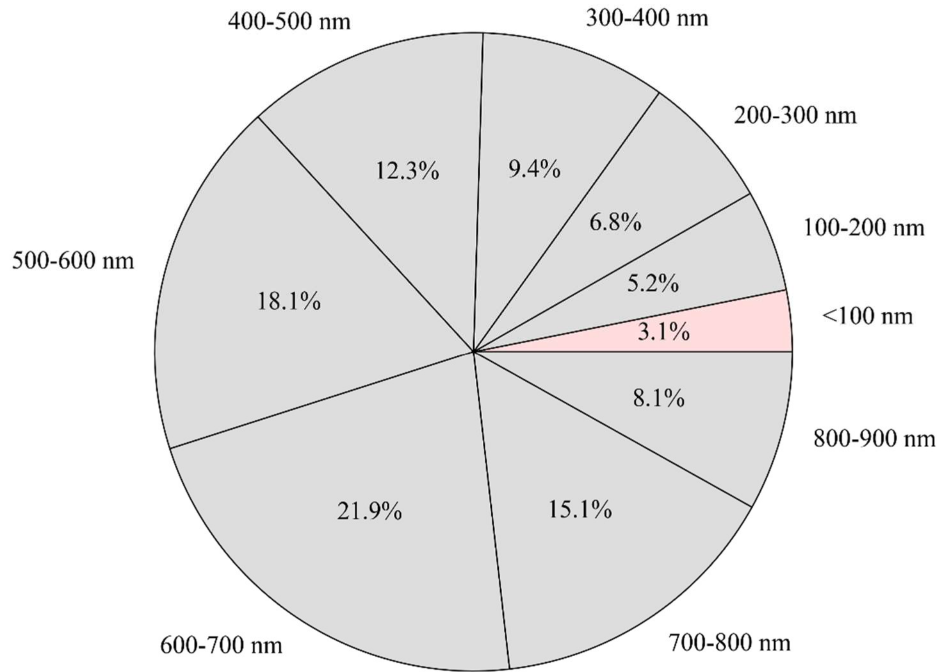

As shown in Figure 4.5, the majority of the particles fall into the sub-100 nm regime of particle diameters. There is more than double the amount of those particles than there are those in the next largest particle size regime (100-200 nm). This is a good indicator that the in situ nanoparticle generation was at least partially successful. On the other hand, there is still a significant number of larger aggregates in the material. Although the histogram of particle sizes seems to indicate a large majority of nanoscale particles, this does not indicate how effectively the silica is being dispersed in the composite. To estimate how effectively the silica is being utilized to produce nanoscale particles, the pixels representing all silica exposed in the image can be grouped into the particle diameter regimes. Then, the silica pixels in each regime can be expressed as a

percentage of the total pictured silica pixels in the image. Plotting the share of the image's total pictured silica pixels in each regime suggests that there is much potential for improvement. In these data shown in Figures Figure 4.5 and Figure 4.6, it can be seen that despite the larger particles being outnumbered significantly, they represent most of the silica in the image. In fact, only approximately 3% of the silica content in the image is contributing to the sub-100 nm particles, whereas nearly 97% of the silica belongs to particles over 100 nm.

This analysis shows very little of the silica in the material actually ends up as part of a nanoparticle of 100 nm or less in size, and therefore the material can be more accurately described as a *microcomposite* instead of a nanocomposite. As discussed in Section 2.7.3, at least one previous study has suggested that the dielectric strength of a composite material can be limited when the filler material is poorly dispersed. It is also generally accepted that the desired enhancement of mechanical properties provided by nano-scale particles depends significantly on the size and dispersion of those particles in the host material. If the particles are large and the filler material not well-dispersed such as in the sample examined in this section, we should expect both limited dielectric strength and limited enhancement of mechanical properties. Further experimentation is required in order to more effectively disperse the available silica content.

4.2 Room Temperature Dielectric Strength

4.2.1 Electrode Simulation

ANSYS Maxwell simulation of the electrode configuration confirmed that the expected electric field applied to a sample is uniform for all points between the contact faces of the electrodes. The electrode geometry, which was selected from the table of

suggestions provided in the ASTM D3755 standard, was reproduced with Maxwell's 3D modeling capability. Details of the 3D model were made to exact specifications, although limitations in manufacturing and measurement capability prevented the real-world electrodes from matching them exactly. Ideally, surface roughness of the contact faces could be measured and then refined, but there was no suitable instrument available to perform this measurement. Similarly, the radius of the electrode's edge fillet suggested in the ASTM standard was approximated during manufacturing, as there were no available methods to precisely verify either their radius or their smoothness.

As shown in Figure 4.7, the simulated electric field through a sample for the electrode configuration used in this work is 196.85 kV/mm when a 5 kV potential difference is applied across a sample that is 25.4 μm thick. This field strength is constant from the center of the electrode contact face to the rounded outer edge of the electrode. Additionally, the direction of the field is expected to be straight through the thickness of the sample, as indicated by the electric field vectors shown in Figure 4.8. These simulation results add confidence to the expectation that the location of a breakdown event has a uniform probability of occurrence across the entire electrode assembly.

Figure 4.7

Simulated Electric Field Strength Across the Electrode Contact Area

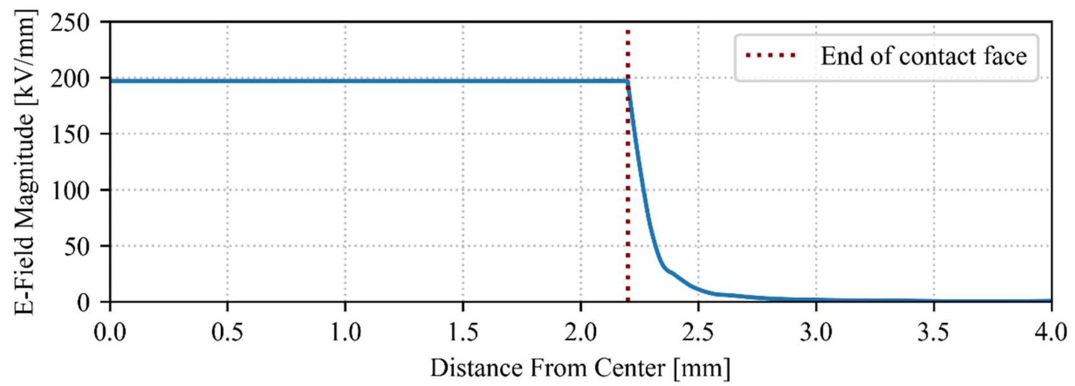

Figure 4.8

Simulated Electric Field for Electrodes Loaded with Polyimide Film

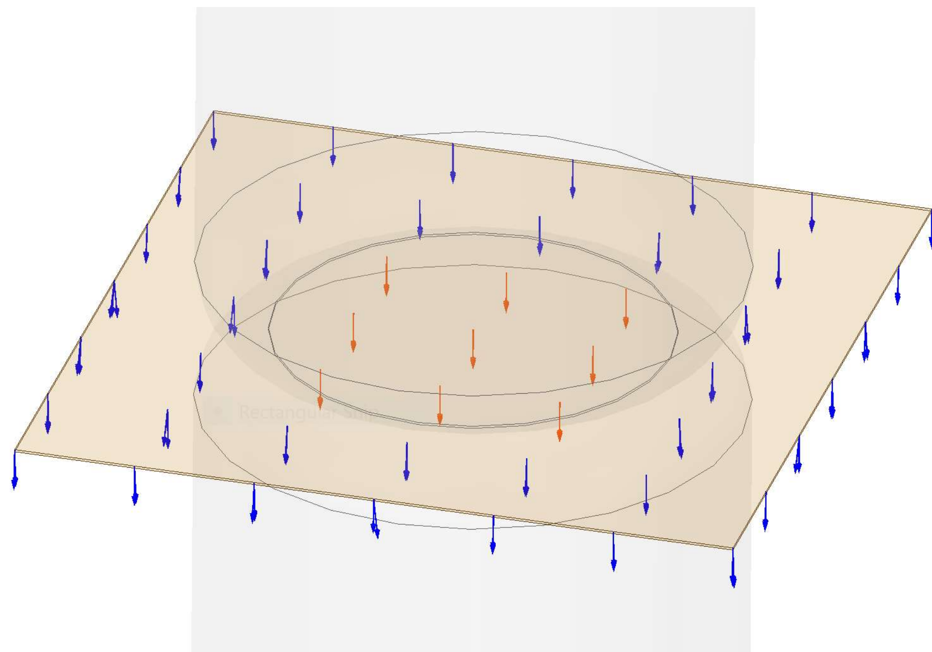

4.2.2 Control Measurements

Dielectric strength measurements on Kapton film were taken periodically as a control. Only data from tests that resulted in breakdown are included in Figure 4.9; any data that did not produce a perforation through the material resulted either in a sparkover, a flashover, or no discharge at all is omitted from the figure. Instead, those tests were used as indicators to improve the electrode-to-sample contact. The median dielectric strength of 296 kV/mm over 27 applicable Kapton measurements is within 2.3% of the datasheet value. The results ranged from a minimum of 267 kV/mm to a maximum of 322 kV/mm.

Figure 4.9

Dielectric Strength for Kapton Film at Room Temperature

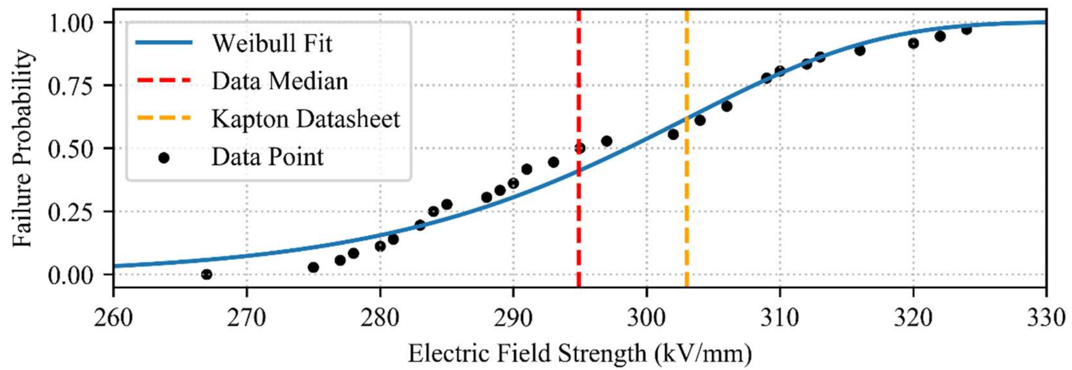

4.2.3 Kapton PI vs. Lab-Made PI

The host matrix for the nanocomposite was evaluated for its dielectric strength in comparison with the Kapton control material. As shown in Figure 4.10, the polyimide made for use as a matrix in nanocomposite films varied more widely and at 270 kV/mm was weaker than Kapton by approximately 10%. It is also clear due to the contrast in

slope between the two curves that the data for the lab-made PI varies significantly more widely. These results are not unexpected, however, because Kapton is a commercially available material made through a well-refined process.

Figure 4.10

Lab-Made Polyimide Dielectric Strength Compared to Kapton

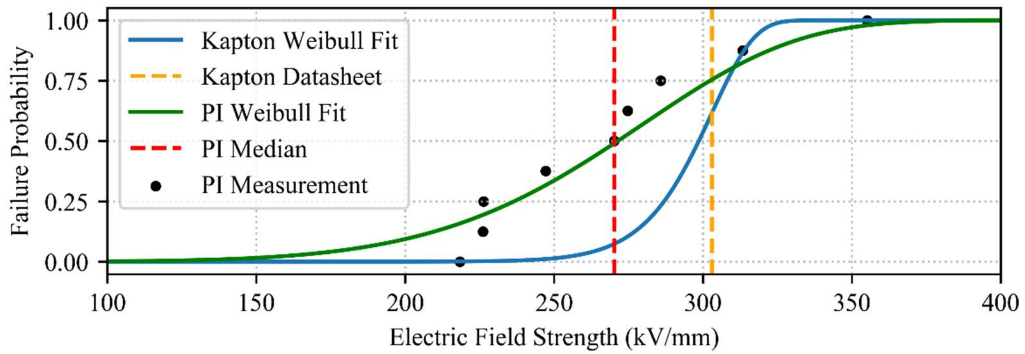

4.2.4 Dielectric Strength vs. Silica Concentration

Dielectric strength data for nanocomposite films with silica concentrations from 0-7% are shown in Figure 4.11. The data shows that with the dielectric strength of the material falls with added silica and is reduced by a maximum of 40% with higher concentrations. There are several explanations for this result in literature.

Figure 4.11

Dielectric Strength vs. Silica Concentration for PI/SiO_2 Films

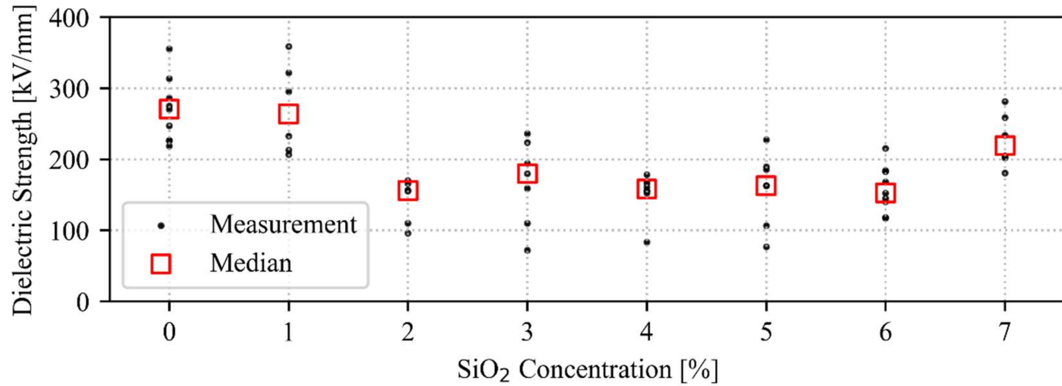

The increased free volume inside interfacial interaction zones between nanocomposite phases has been suggested to have a role in the dielectric strength of nanocomposites. These interfacial regions allow for increased electron mobility and thus greater electron acceleration relative to the bulk material given the same applied electric field. Should the electric field be strong enough to release an electron from the polymer matrix into the interfacial region, the freed electron would then be able to gain energy while being accelerated by the electric field through the free volume. For nanoscale particles it may be that the energy gained during acceleration is only enough to dissipate as heat in the material. However, with high enough concentrations of filler it is possible that the interfacial regions of two or more particles overlap. In this case, the distance over which an electron can accelerate can be increased such that it gains significant energy. Upon reuniting with the matrix material, it may have gained enough energy to cause significant thermal damage or potentially an avalanche breakdown. A highly simplified example can be seen in Figure 4.12, which shows how higher particle concentrations can

increase the likelihood of overlapping interfacial regions, which in turn can increase the path for electron acceleration.

Figure 4.12

Paths of Acceleration Through Interfacial Regions around Filler Particles

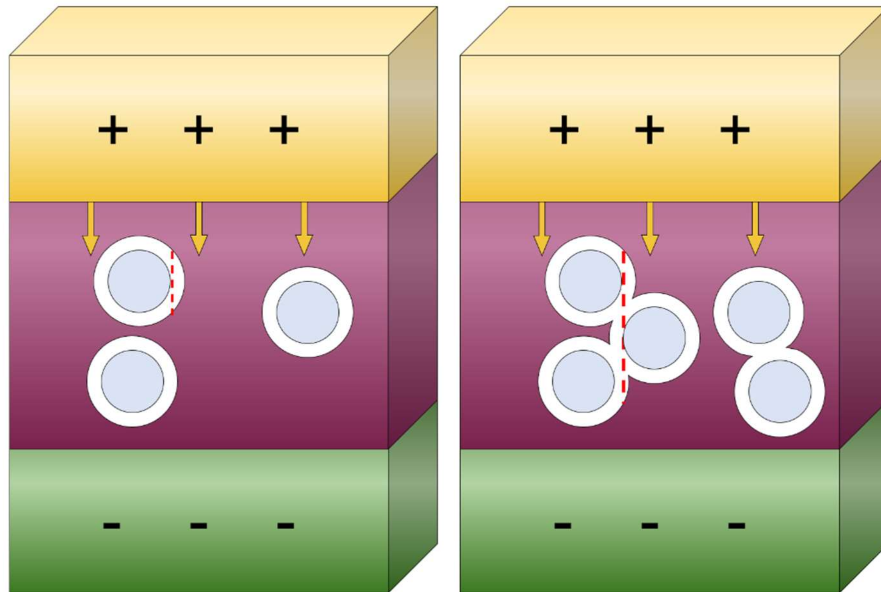

It is also known that composite materials in which the matrix and filler materials have differing dielectric constants will distort and enhance the electric field at filler particle boundaries. For these materials the electric field enhancement can lead to partial discharge and ultimately dielectric breakdown. This is especially so in cases where the filler material has a lower dielectric strength than the bulk material, and where the filler particles are of microscale rather than nanoscale dimensions. Both of these conditions are satisfied based on the known properties of silica and the SEM analysis discussed in Section 4.1.1.

4.2.5 Breakdown Microscopy

Images captured during optical microscopy of breakdown locations may provide additional insight into the nature of dielectric failures in PI/SiO_2 nanocomposites. Perforations created during failures consisted of two regions of interest: an inner circle presumed to be a clear hole through the thickness of the material, and an outer ring, damaged though not completely removed. Figure 4.13 shows these two regions highlighted. To verify that the inner breakdown region is punctured through the entire thickness, SEM imaging was performed for a selection of the samples. The areas suspected to be punctured through completely were revealed as such in the SEM images shown in Figure 4.14.

Figure 4.13

Inner (left) and Outer (right) Regions of a Dielectric Breakdown Puncture

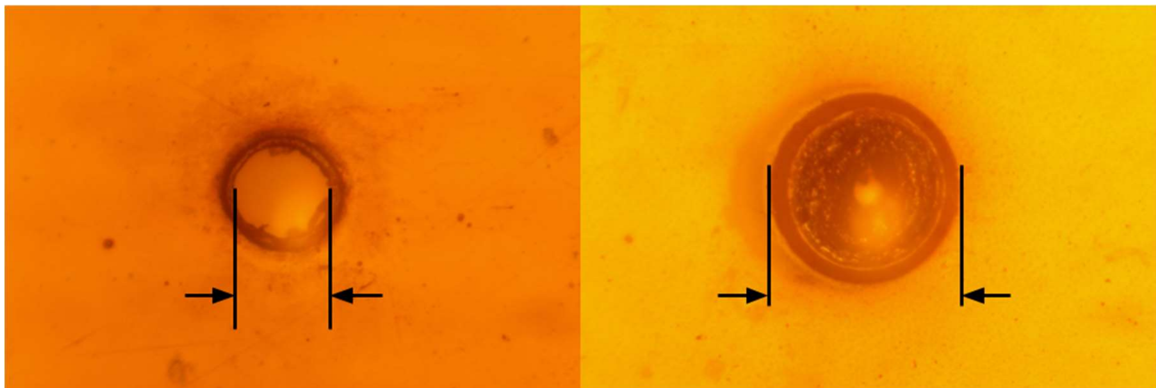

Figure 4.14

SEM (left) and Optical (right) Captures of a Dielectric Breakdown Puncture

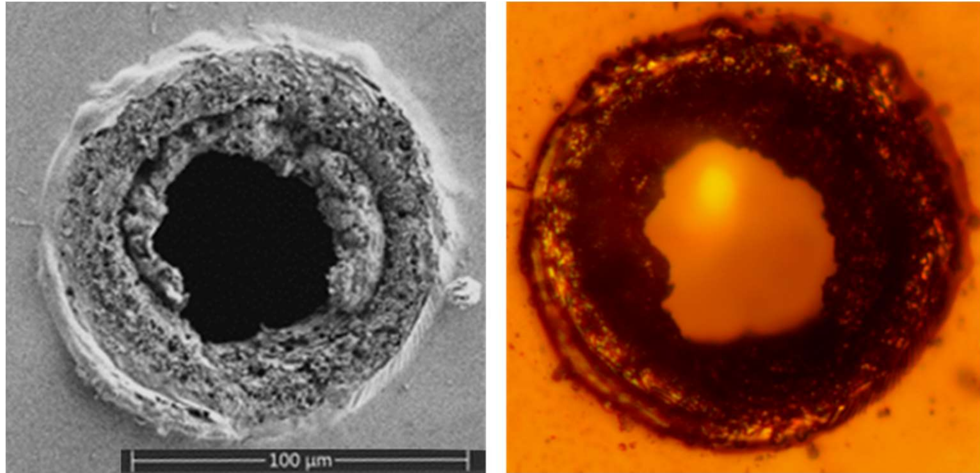

4.2.6 Geometric Analysis of Perforation Regions

The breakdown perforations were measured for their sizes and compared in a number of contexts to examine any potential correlation between puncture morphology and other parameters. A distinct correlation was found between the inner breakdown region's diameter and the concentration of SiO_2 in the material. This relationship, shown in Figure 4.15, suggests that the diameter of the hole produced by a dielectric breakdown has an inverse relationship with the concentration of silica nanoparticles. That is, the largest holes generally appeared in the pure PI samples, and the size of the perforations became smaller with added silica content.

Figure 4.15

Dielectric Breakdown Hole Size Against SiO_2 Concentration

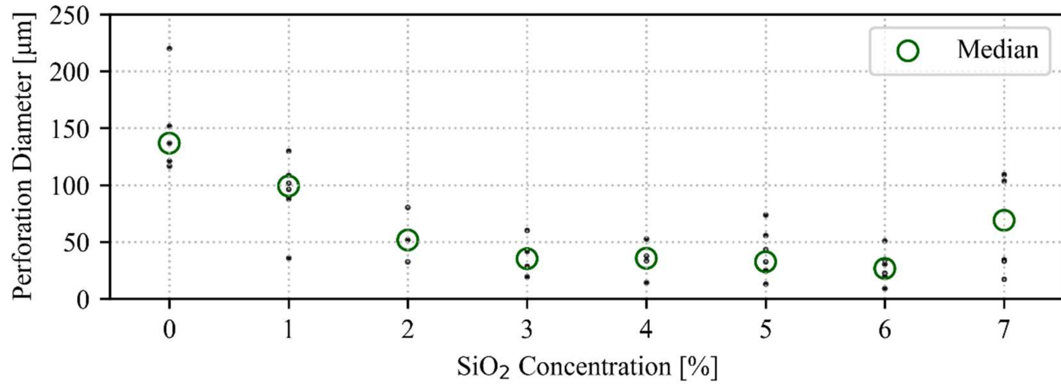

In order to rule out other possible correlations that may influence the appearance of this possible relationship, the hole diameter measurements were also plotted against dielectric strength, breakdown voltage, and sample thickness for each measurement. These plots are displayed in Figure 4.16. The plots are mostly unclear, although there is the appearance of a potential relationship between hole size and dielectric strength and/or breakdown voltage. They also somewhat reinforce the relationship suggested in Section 4.2.4, in which the 1% silica samples exhibit greater dielectric strength than the other composites. With this, a direct relationship between filler concentration and perforation diameter has not been disproved, and filler concentration is not confounded with any of the other three variables examined.

Figure 4.16

Hole Size vs. Dielectric Strength, Breakdown Voltage, and Sample Thickness

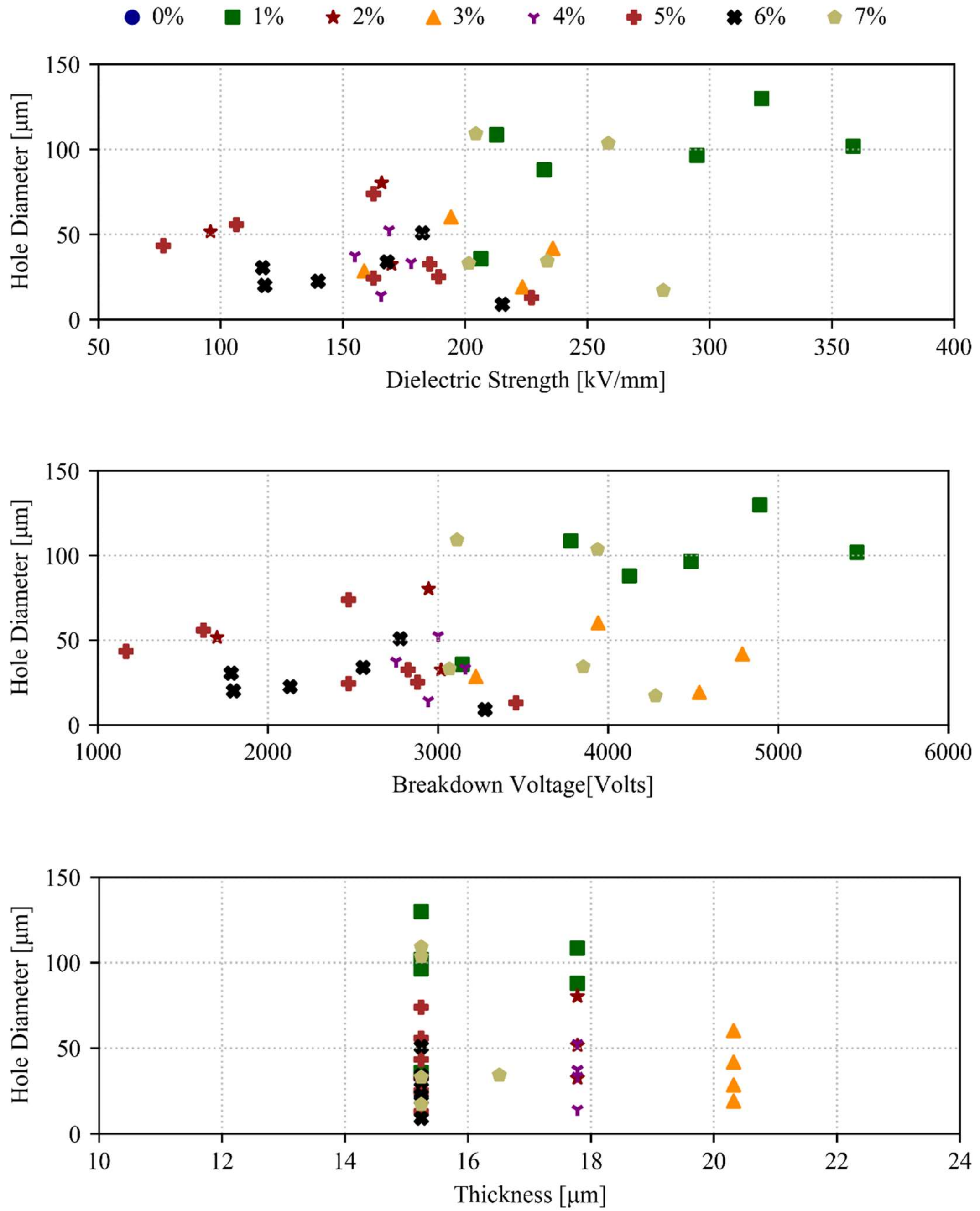

4.3 Low Temperature Dielectric Strength

4.3.1 Low Temperature Control Measurements

Kapton was again used as a control to verify the measurement capability of the low temperature test system. The results are can be seen in Figure 4.17 and show good agreement with datasheet values.

Figure 4.17

Dielectric Strength for Kapton Film at Low Temperatures

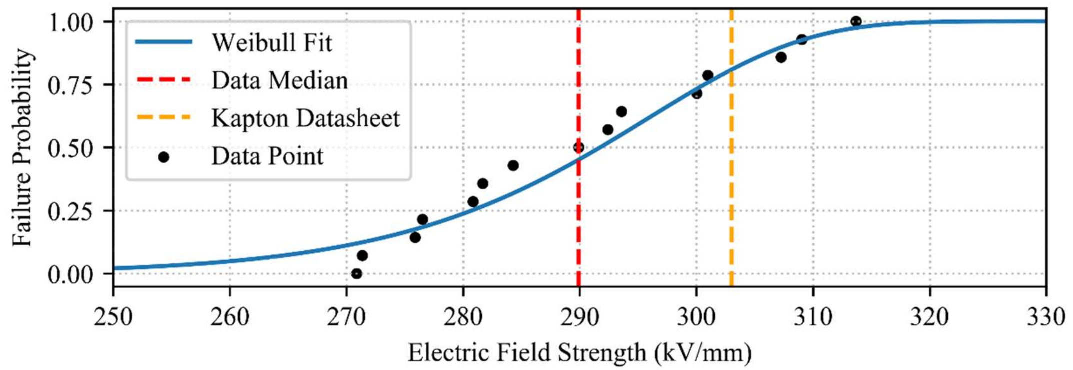

4.3.2 Low Temperature Nanocomposite Dielectric Strength

The data collected from dielectric strength measurements near liquid nitrogen temperatures are shown in Figure 4.18. The inverse relationship between filler concentration and dielectric strength exhibited for room temperature testing did not reappear for low temperature measurements. The exception is for the 2% data set, which also has by far the widest spread and therefore the largest uncertainty. This large uncertainty leaves open the possibility that there is in fact a less severe or nonexistent decrease in dielectric strength at low temperature with higher SiO_2 concentrations.

Figure 4.18

Results of Low Temperature Dielectric Strength Testing

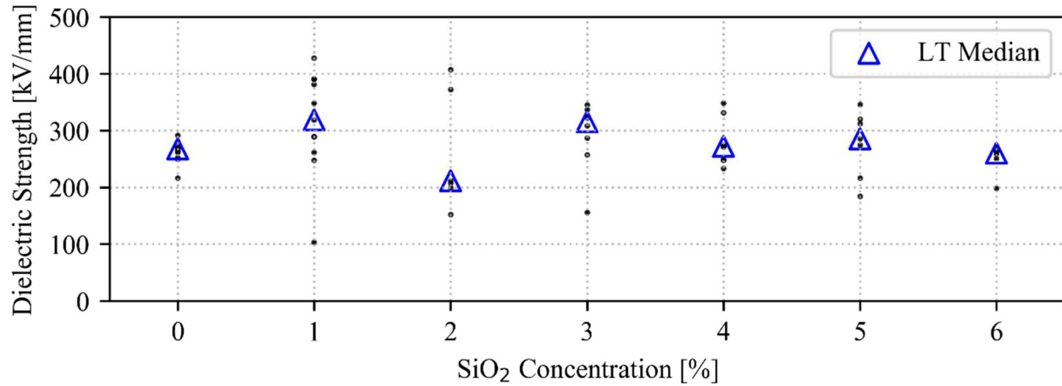

4.3.3 Dielectric Strength vs. Silica Concentration vs. Temperature

When directly compared to the room temperature dielectric strength data, the data indicates that all PI/SiO_2 nanocomposites saw a significant increase in dielectric withstand capability at cryogenic (90 K) temperatures. Table 4.1 and Figure 4.19 show the median dielectric strength for room temperature and cryogenic temperature testing (with measurement counts in parentheses). Although the pure PI showed no improvement at low temperatures, dielectric strength was increased slightly in composites with lower nanoparticle concentrations and more significantly in those with higher concentrations. Also of note is the increase in the variability of the data for pure PI as well as 1% and 2% nanocomposites at low temperature compared to room temperature as shown in Figure 4.20.

Table 4.1

Dielectric Strength at Room and Low Temperature

Silica Concentration [%]	Room Temperature [kV/mm]	Low Temperature [kV/mm]	$\frac{LT}{RT}$
0	270 (9)	267 (12)	0.99
1	264 (6)	318 (11)	1.21
2	156 (6)	211 (7)	1.36
3	180 (7)	315 (8)	1.76
4	158 (8)	272 (9)	1.72
5	163 (7)	285 (7)	1.76
6	152 (9)	260 (6)	1.71

Figure 4.19

Comparison Between Low-Temperature and Room-Temperature Results

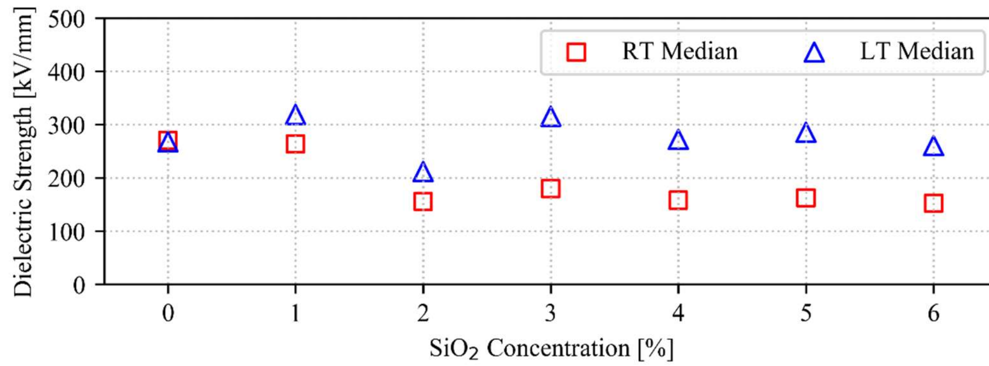

Figure 4.20

Standard Deviation for Dielectric Strength Measurements

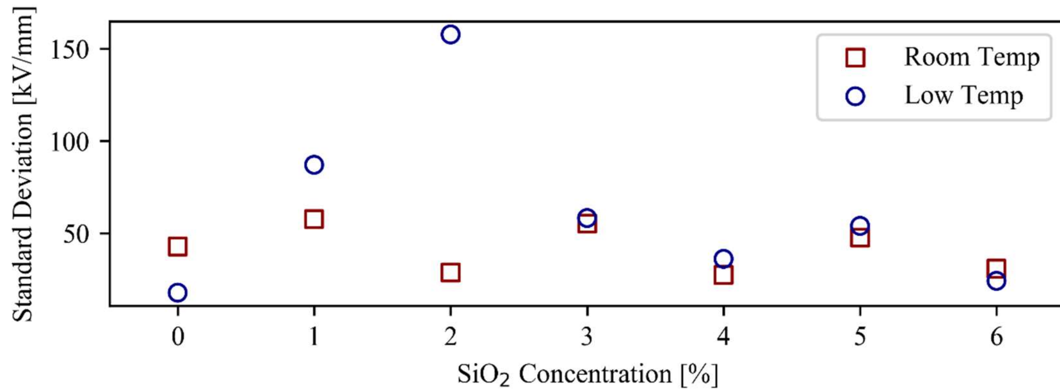

First, it is important to examine for coincidental causes for an increased dielectric strength. For one, if the samples tested at low temperature were significantly thinner on average, then the dielectric strength for those samples could be inflated. However, the thickness measurement data do not suggest that this was the case. It may also be possible that some of the relationships highlighted in the literature review of this work (Section 2.7) could be responsible for this result. Specifically, it is possible that the material generation technique happened to improve over time, and that the particle dispersion was better for the samples prepared later for low temperature testing.

A number of other explanations which are not mutually exclusive are possible for the increase in dielectric strength exhibited by the samples that underwent low temperature testing. From an electrical perspective, it is likely that the same mechanisms considered as an explanation for the room temperature dielectric strength results are still valid possibilities. In a low temperature context, however, there may also be considerable differences in the polymer's free volume that change the probability of breakdown. It has

been shown that the amount of free volume in the interfacial regions of composites can increase with warmer temperatures [54]. If the opposite occurs with low temperatures, reduced free volume in the interfacial regions surrounding filler particles can eliminate some of the overlapping interaction zones described in Section 4.2.4. With fewer of these overlaps, it is likely that damage due to partial discharge would accumulate less severely, and breakdown would require greater or more prolonged electrical stress.

4.3.4 SEM Imaging of Low Temperature Dielectric Failures

Some samples were examined with an SEM after being subject to dielectric testing. The results, shown in Figure 4.21, appear to not have a main perforation going through the entire sample as did the failures created at room temperatures. Instead, the entire damaged area appears similar to the outer regions of the room temperature failures: full of small fractures and punctures. It also appears that there is a circular area of removed material covering the entire damaged region.

Figure 4.21

Breakdown Holes Formed at Room (top) and Low Temperatures (middle, bottom)

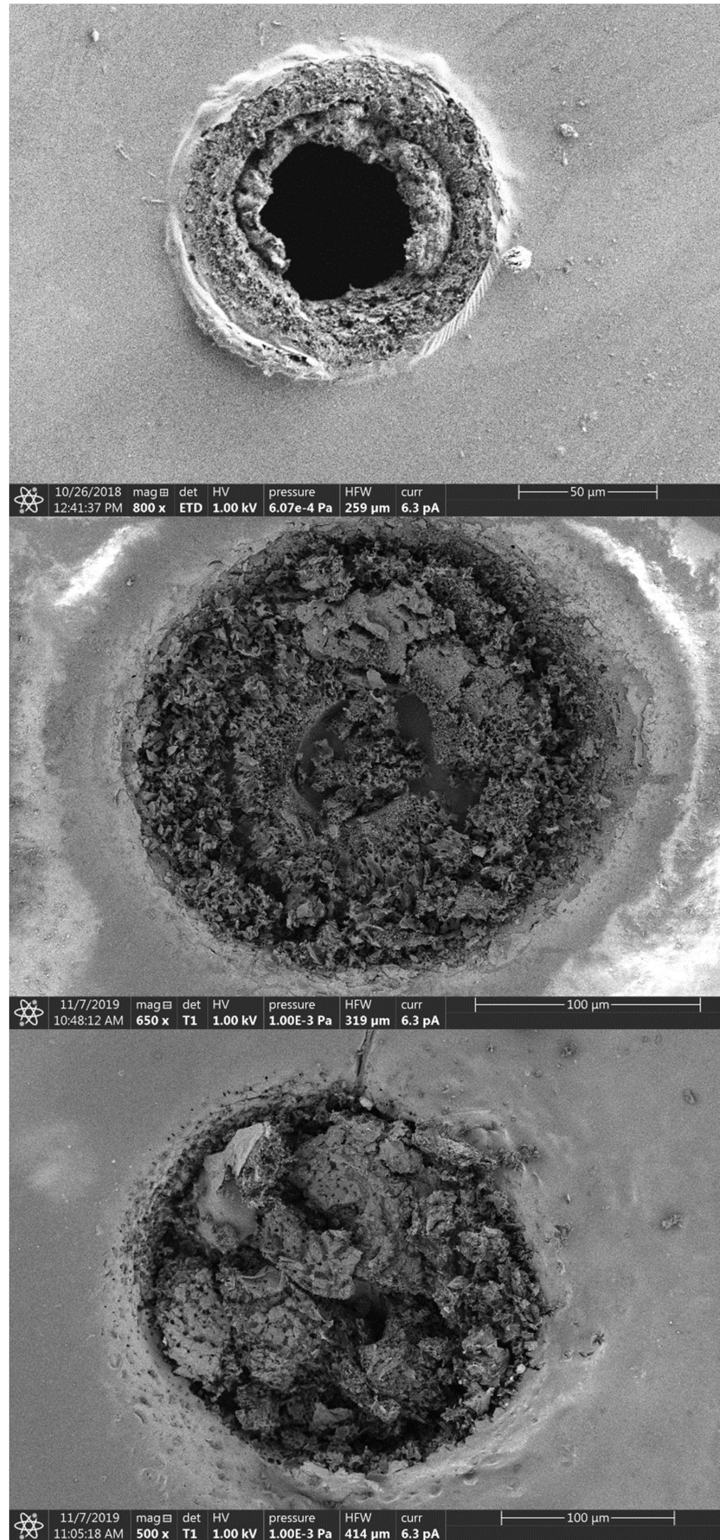

These images may suggest that the material is protected in some ways by the low-temperature environment from thermal damage during the discharge period. There is some nonzero time that the hipot tester takes to discharge after the detection of breakdown currents. In this time, there is energy still being supplied to the damaged sample. Some of this energy is dissipated as heat in the conductive channels formed during the breakdown process. Without the sufficient means of being dispersed, the heat may cause additional damage to the sample. In the low-temperature environment, however, it may be that the lack of heat in the material and the surrounding environment allows the sample to dissipate heat much more readily before reaching the threshold of thermal damage. If this is the case, it is then possible that the limited accumulation of heat near the point of breakdown prevents the creation of a large hole as seen in the samples broken down at room temperature.

This leads to another potential explanation for the increased dielectric strength at low temperatures. The increased capacity to accept and dissipate heat in low temperature environments may protect the material from damage during partial discharges, which generate heat as they occur. At low temperatures, the sample is perhaps less severely damaged by partial discharges, and so it can survive longer into the dielectric strength test without experiencing a full dielectric breakdown.

4.4 Recommendations for Future Work

4.4.1 Nanocomposite Generation

It has been shown in previous studies that nanoparticle morphology in some finished nanocomposites has a significant effect on the dielectric strength of the material.

Particle dispersion and size are important factors in producing effective nanocomposite dielectrics.

The sample examined to capture the data in Figure 4.16 had most of its silica content contributing to particles over 500 nm in diameter. It has been shown that maximization of the interfacial surface area is a key to high-performance nanocomposites as well as a means of boosting the dielectric strength. It could be beneficial to try some common methods for limiting the creation of large silica aggregates. These methods include particle surface treatment and different mixing techniques.

Ex-situ composite generation was also briefly explored but was opted against due to unacceptable formation of silica into large agglomerates. Investigation into particle surface treatments and other methods for improving silica dispersion were limited. Additional investment into ex-situ processes for composite generation may be warranted.

4.4.2 Spin Coating

The average thickness of the 118 film samples represented in this work was 17.95 µm. The uncertainty introduced due to the 1 micrometer thickness resolution is approximately 5.6% for a film of average thickness. The thinnest samples created during this research measured 10.2 µm. For these films, the uncertainty of the testing results due to the thickness alone reaches almost 10%. On the other hand, thickness measurement on a sample of 25 µm thickness would reduce this uncertainty to 4%. The hipot tester used in this work can apply up to 10 kV to the films, and most films broke down with less than half of that. If the average film thickness were increased to 20-25 µm, the measurement

uncertainty would be decreased, and the system would still be able to break samples down.

During thickness measurements, it was observed that the repeatability of the micrometer used could be improved. Thickness measurements would likely be more reliable if the operator error were mitigated through the use of a thickness gauge with a lever, rather than a manual spindle. With the use of the lever the compressive force is controlled. This is unlike a micrometer with a manual spindle that is opened and closed with a thumb and can produce widely varying measurements on the same film.

Once the measurement is more reliable, it would also be helpful to reduce the variability of the sample thicknesses by auditing and improving the spin-coating process. As described in the discussion of partial discharge as a breakdown mechanism (Section 2.4.2, thicker samples are more likely to have impurities which can cause a lower measured breakdown strength, while materials exhibit dielectric strength closer to the maximum intrinsic value as thickness decreases. Because of this relationship between measured field strength at breakdown and sample thickness, it is important to have a consistent spin-coating outcome. By improving the spin-coating and thickness measurement processes, it is possible to greatly improve the accuracy of the results.

4.4.3 Dielectric Strength Testing

The standard adhered to during the dielectric testing in this research requires that a 50 g force is applied by the upper electrode assembly to the sample. This is to ensure reliable contact between the specimen and the electrode faces. While the room temperature testing system was engineered to have a 50 g mass for the upper assembly,

the guide rails that aligned it with the lower assembly were a possible source of friction. The friction between the upper assembly and its guide rails could have worked against gravity, reducing the contact force and potentially inflating the resulting breakdown voltage. This issue emerged more severely in the LN electrode assembly. It was not uncommon for a test not to result in breakdown after several minutes of cooling. When the electrode assembly was pulled from the dewar in such cases, the upper electrode would be completely separated from the sample.

The electrode assembly design should again be revisited to achieve a more reliable electrode contact force. It may be possible to alleviate this issue with a spring-loaded system. A spring with a known spring constant would have a known deflection under a compressive load of 50 g, and this could be leveraged to apply a known contact force to the samples. It will be vital to eliminate this issue before helium testing, which will consume large amounts of time to achieve the target test temperatures.

There are still tests which can be revealing at room and LN temperatures and can be achieved with little or no additional equipment needed. One such test would require the sample to be held at a steady voltage slightly below the expected breakdown voltage. This would provide insight into the long term dielectric withstand capability of the material. Also, the dielectric strength of the material should be monitored after increasing numbers of thermal cycles. As the material is cooled, allowed to return to room temperature, and cooled again, it may be going through changes which affect its dielectric strength. Both of these tests are vital to understanding how this material may perform in HTS cable applications.

4.4.4 Helium-Cooled Dielectric Strength Tests

The results of this work suggest that the dielectric withstand capability of PI/SiO_2 nanocomposites is not adversely affected by low temperatures. The data in fact shows that it may improve this feature of the material. Because the film performs electrically better under low-temperature conditions, and because the helium testing will likely take very long times to reach target temperatures for testing, the nanocomposite loading concentration should be optimized only for CTE. In other words, only CTE testing should be performed with the helium chamber at first. If and when a particle concentration has been found to produce the desired CTE result, that material can be tested to verify that the dielectric strength is sufficient for the application. The results of this work suggest that it will likely be so.

Chapter 5

Conclusion

Dielectrics are a critical component of the high-temperature superconductor cables used in many vital technologies. Emerging needs for increasing current densities in HTS cables have necessitated colder environments than liquid nitrogen can provide. New strategies for insulating superconducting layers are being developed to support the gaseous helium coolant which can reach the required temperatures. One such strategy is an extruded polymer coating which must be engineered to match the coefficient of thermal expansion of an HTS cable's core. Nanocomposites offer one possible path toward this material. Specifically, polyimide/silicon dioxide nanocomposites are a promising method of fulfilling the dielectric needs of new HTS cables. Any material engineered for use as an electrical insulator has a number of vital properties which determine its suitability for its intended application. Dielectric strength—a material's capability to withstand electric fields—is one of these properties.

In this work, PI/SiO_2 nanocomposites with nanoparticle concentrations between 1 and 7% were tested for their dielectric strength at room temperature and at temperatures near the boiling point of liquid nitrogen. The materials were generated through an in situ process and cast to films between 10 and 26 micrometers thick. The results showed a decrease in dielectric strength at room temperature as the nanoparticle load was increased. However, at low temperatures, all samples with nanoparticles were electrically stronger than similar ones tested at room temperature. In addition, the decrease in dielectric strength with additional particle loading was eliminated at low temperatures. This result could potentially be explained by a combination of two consequences of the

low temperature. First, the contraction due to cold possibly mitigates the likelihood of overlapping free volumes in interfacial layers between polymer and silica phases which would typically cause breakdown at room temperature. Also, the low temperature condition of the sample and environment may delay the damage normally caused from heat generated during partial discharges. Ultimately, at low temperature, all of the materials tested demonstrated exceptional dielectric withstand capabilities which would be well-suited for use in HTS cables.

References

[1] D. V. Delft and P. Kes, "The Discovery of Superconductivity," *Physics Today,* vol. 63, pp. 38-43, 2010.

[2] R. Prozorov, "The Phenomenon of Superconductivity and Fundamental Properties," in *Ullmanns Encyclopedia of Industrial Chemistry*, 2016, pp. 1-9.

[3] O. o. T. A. Congress of the U.S., "High Temperature Superconductivity in Perspective," 1990.

[4] R. Kleiner and W. Buckel, "Applications of Superconductivity," in *Superconductivity: An Introduction*, John Wiley & Sons, 2016, p. 373–476.

[5] K. Ijagbemi, "Sustainable Power Technology: A Viable Sustainable Energy Solution," *Skills Development for Sustainable Manufacturing,* 2017.

[6] S. L. et al., "Digital Logic Gates Using Hot-Phonon Controlled Superconducting Nanotransistors," *IEEE Transactions on Appiled Superconductivity,* vol. 13, pp. 1104-1106, 2003.

[7] B. M. et al., "Development of Superconductive Microwave Filters for Mobile Communications and Filter Banks," *IEEE Transactions on Appiled Superconductivity,* vol. 9, pp. 4014-4017, 1999.

[8] K. M. Davies, P. J. Norman, C. E. Jones, S. J. Galloway and G. M. Burt, "Fault Behaviour of a Superconducting Turboelectric Distributed Propulsion Aircraft Network: A Comprehensive Sensitivity Study," *2015 International Conference on Electrical Systems for Aircraft, Railway, Ship Propulsion and Road Vehicles (ESARS),* 2015.

[9] R. Hott, "Application Fields of High-Temperature Superconductors," *High Temperature Superconductivity 2,* p. 35–48, 2004.

[10] S. Pamidi, C. H. Kim and L. Graber, "High-temperature Superconducting (HTS) Power Cables Cooled by Helium Gas," *Superconductors in the Power Grid,* pp. 225-260, 2015.

[11] P. Lee, "Superconducting Wires and Cables: Materials and Processing"*,* 2003, pp. 1-11.

[12] J. G. Bednorz and K. A. Müller, "Possible High Tc Superconductivity in the Ba-La-Cu-O System," *Z. Physik B - Condensed Matter,* vol. 64, pp. 189-193, 1986.

[13] B. Keimer, S. A. Kivelson, M. R. N. amd S. Uchida and J. Zaanen, "From Quantum Matter to High-temperature Superconductivity in Copper Oxides," *Nature,* vol. 518, p. 179–186, 2015.

[14] Z. Melhem, High Temperature Superconductors (HTS) for Energy Applications, Oxford: WP, Woodhead Publ., 2012.

[15] P. Chaddah, "Critical Current Densities in Superconducting Materials," *Sadhana,* vol. 28, pp. 273-282, 2003.

[16] L. Graber, C. H. Kim, S. V. Pamidi, H. Rodrigo and D. Knoll, "Dielectric Design Validation of a Helium Gas Cooled Superconducting DC Power Cable," *IEEE Electrical Insulation Conference (EIC),* 2014.

[17] O. Tonnesen and J. Ostergaard, "High Temperature Superconducting Cables," in *High Temperature Superconductivity 2*, Springer, 2004, pp. 537-567.

[18] L. Graber, C. H. Kim, S. V. Pamidi, H. Rodrigo and D. Knoll, "Dielectric Design Validation of a Helium Gas Cooled Superconducting DC Power Cable," in *2014 IEEE Electrical Insulation Conference (EIC)*, 2014, pp. 157-161.

[19] A. K. Vijh, "Relative Electric Strengths and Polarizabilities of Gaseous Dielectrics," *Materials Chemistry and Physics,* vol. 12, pp. 287-296, 1985.

[20] A. Bondi, "Van der Waals Volumes and Radii," *The Journal of Physical Chemistry,* vol. 68, pp. 441-451, 1964.

[21] R. A. S. J. W. Jewett, Physics for Scientists and Engineers, 8th ed., USA: Brooks/Cole Publishing Co., 2011.

[22] Y. Nakajima, H. Janaka, K. Mochizuki, K. Fuse, Y. Arashitani, T. Nishimoto, A. Seno and M. Okada, "A Study for Estimating Thermal Strain and Thermal Stress in Optical Fiber Coatings," *Furukawa Review,* pp. 8-12, October 2008.

[23] R. Elhajjar, V. L. Saponara and A. Muliana, Smart Composites, 1st ed., USA: Boca Raton: CRC Press, 2014.

[24] W. Liu, B. Zhu, J. Zhang and Y. Xu, "Preparation and Dielectric Properties of Polyimide/Silica Nanocomposite Films Prepared from Sol–gel and Blending Process," *Polymers for Advanced Technologies,* vol. 18, pp. 522-528, 2007.

[25] L. Weng, H. Li, X. Yang and L. Liu, "Preparation and Characterization of Silica/Polyimide Nanocomposite Films Based on Water-soluble Poly(amic acid) Ammonium Salt," *Polymer Composites,* vol. 38, pp. 774-781, 2017.

[26] C. C. Okpala, "The Benefits and Applications of Nanocomposites," 2014.

[27] M. C. Porter, "Superconductivity/YBCO," *IEEE Potentials,* vol. 15, pp. 30-35, 1996.

[28] A. Drozdov, P. Kong, V. Minkov, S. Besedin, M. Kuzovnikov, S. Mozaffari, L. Balicas, F. Balakirev, D. Graf, V. Prakapenka, E. Greenberg, D. Knyazev, M. Tkacz and M. Eremets, "Superconductivity at 250 K in lanthanum hydride under high pressures," *Nature,* vol. 569, pp. 528-531, May 2019.

[29] D. Czerwinski, Modelling the critical parameters of high temperature superconductor devices in transient states, 2013.

[30] “Transmission cables - superconducting wire by sti - conductus®,” accessed: 19-Apr-2020. [Online]. Available: https://www.suptech.com/transmission-cables/

[31] A. P. Malozemoff, J. Yuan and C. M. Rey, "High-temperature superconducting (HTS) AC cables for power grid applications," in *Superconductors in the Power Grid*, C. Rey, Ed., Woodhead Publishing, 2015, pp. 133-188.

[32] U. S. G. Survey, *Historical Statistics for Mineral and Material Commodities in the United States: U.S. Geological Survey Data Series 140,* 2014.

[33] M. S. Naidu and V. Kamaraju, High Voltage Engineering, 3rd ed. ed., Tata McGraw-Hill,, 2006.

[34] "Standard Test Method for Dielectric Breakdown Voltage and Dielectric Strength of Solid Electrical Insulating Materials Under Direct-Voltage Stress," 2014.

[35] P. H. F. Morshuis and J. J. Smit, "Partial discharges at DC voltage: their mechanism, detection and analysis," *IEEE Transactions on Dielectrics and Electrical Insulation,* vol. 12, pp. 328-340, 2005.

[36] C. L. Wadhwa, High voltage engineering, New Age, 2004.

[37] Y. Davydov, "On the First Townsend Coefficient at High Electric Field," *IEEE Transactions on Nuclear Science,* vol. 53, pp. 2931-2935, 2006.

[38] K. Burm, "Calculation of the Townsend Discharge Coefficients and the Paschen Curve Coefficients," *Contributions To Plasma Physics,* vol. 47, pp. 177-182, 2007.

[39] S. Radwan, H. El-Khabeary and A. Helal, "Study the Secondary Electron Emission Coefficient using Disc and Conical Electrodes," *Canadian Journal of Physics,* vol. 94, September 2016.

[40] T. Burton, T. Back, S. Fairchild and G. Thompson, "Influence of surface roughness on secondary electron emission from graphite," *Journal of Vacuum Science & Technology A: Vacuum, Surfaces, and Films,* vol. 35, July 2017.

[41] N. Heckert, J. Filliben, C. Croarkin, B. Hembree, W. Guthrie, P. Tobias and J. Prinz, *Handbook 151: NIST/SEMATECH e-Handbook of Statistical Methods,* NIST Interagency/Internal Report (NISTIR), National Institute of Standards and Technology, Gaithersburg, MD, 2002.

[42] J. Ekin and G. Zimmerman, "Experimental Techniques for Low-Temperature Measurements: Cryostat Design, Material Properties, and Superconductor Critical-Current Testing," *Physics Today - PHYS TODAY,* vol. 60, May 2007.

[43] W. Chen, W. Chen, B. Zhang, S. Yang and C.-Y. Liu, "Thermal imidization process of polyimide film: Interplay between solvent evaporation and imidization," *Polymer,* vol. 109, pp. 205-215, 2017.

[44] “Silica - silicon dioxide (sio2),” accessed: 30-Mar-2021. [Online]. Available: https: //www.azom.com/article.aspx?ArticleID=1114

[45] W. Stöber, A. Fink and E. Bohn, "Controlled growth of monodisperse silica spheres in the micron size range," *Journal of Colloid and Interface Science,* vol. 26, pp. 62-69, January 1968.

[46] J. K. Nelson and J. C. Fothergill, "Internal Charge Behavior of Nanocomposites," *Nanotechnology,* vol. 15, pp. 586-595, 2004.

[47] O. Gallot-Lavallée, V. Griseri, G. Teyssedre and C. Laurent, "The pulsed electro-acoustic technique in research on dielectrics for electrical engineering Today's achievements and perspectives for the future," *Revue internationale de génie électrique,* vol. 8, pp. 749-772, September 2005.

[48] G. Polizos, E. Tuncer, I. Sauers and K. L. More, "Properties of a Nanodielectric Cryogenic Resin," *Applied Physics Letters,* vol. 96, p. 152903, 2003.

[49] X. Cui, G. Zhu, W. Liu, K. Wang, F. Ren, H. Fu and X. Yan, "Mechanical and Dielectric Properties of Polyimide/Silica Nanocomposite Films," *Plastics, Rubber and Composites,* vol. 44, pp. 435-439, 2015.

[50] H. Zhang, G. Zhang, R. Tan, M. Luo and Y. Tu, "Study on DC Breakdown Characteristics of Polyimide at Cryogenic Temperature," in *2012 Asia-Pacific Power and Energy Engineering Conference*, 2012.

[51] A. Hossam-Eldin, "Electric Strength of Polymers Under Vacuum at Cryogenic Temperatures," *International Journal of Polymeric Materials,* vol. 10, pp. 293-302, January 1984.

[52] H. M. Hones, "Polyimide/silicon dioxide nanocomposites as dielectrics for helium-cooled high-temperature superconducting cables," *Theses and Dissertations,* vol. 2817, 2020.

[53] *MATLAB Image Processing Toolbox,* 2018.

[54] Y. Yang, H. Jinliang, G. Wu and J. Hu, "Thermal Stabilization Effect of Al2O3 nano-dopants improves the high-temperature dielectric performance of polyimide," *Scientific Reports,* vol. 5, p. 16986, November 2015.